Thesis for the degree of doctor of philosophy

Building a Bosonic Microwave Qubit

Marina Kudra

CHALMERS
UNIVERSITY OF TECHNOLOGY

Department of Microtechnology and Nanoscience - MC2
Quantum Technology Laboratory
Chalmers University of Technology
Göteborg, Sweden 2023

Building a Bosonic Microwave Qubit

MARINA KUDRA

ISBN 978-91-7905-780-0

© MARINA KUDRA, 2023.

Doktorsavhandlingar vid Chalmers tekniska högskola
Ny serie nr. 5246
ISSN 0346-718X

Quantum Technology Laboratory
Department of Microtechnology and Nanoscience- MC2
Chalmers University of Technology
SE-412 96 Göteborg, Sweden
Telephone +46 31 772 1000

Cover: Wigner-negative bosonic states "living" inside a 3D superconducting cavity. The Wigner functions are the experimental data of states created in papers IV and VI.

Printed by Chalmers digitaltryck
Göteborg, Sweden 2022

Building a Bosonic Microwave Qubit

MARINA KUDRA
Department Microtechnology and Nanoscience
Chalmers University of Technology
Göteborg, Sweden 2023

Abstract

Superconducting circuits is a promising platform for quantum computing. Quantum information is usually stored in discrete two-level qubits e.g. in transmon qubits. These qubits are interconnected and placed in grids to form logical qubits, and many logical qubits together form a quantum computer.

In this thesis, we consider encoding quantum information in a resonator instead of the two-level qubit. Resonators can host bosonic modes that have, in principle, an infinite number of quantum levels in which we redundantly can encode a discrete qubit. This makes bosonic qubits hardware efficient, since we can perform error correction directly on a single hardware component, namely the resonator. However, we will still need to use an ancilla two-level qubit to universally control the bosonic qubit. This thesis can be interpreted as an instruction guide on creating a bosonic microwave qubit and it contains the following chapters.

We first introduce the cryogenic setup and the state-of-the-art room-temperature hardware that generates the microwave pulses we need to perform all the experiments in this thesis. We discuss the latest generation of the room-temperature measurement- and control-system we used for both bosonic and discrete variable qubit systems.

We then introduce the hardware components that are needed to form a bosonic qubit, namely a superconducting transmon qubit and a 3D superconducting cavity. We explore the fluctuations of their coherence properties, and we try to understand the sources of noise that limit those properties.

Next, we create arbitrary bosonic states and gates by using interleaved sequences of displacements and optimized selective number-dependent arbitrary phase gates. We characterize a bosonic gate, the X-gate on the binomially encoded qubit, by coherent state process tomography.

We then characterize the selective photon addition gate. We implement this gate by a comb of off-resonant drives that simultaneously excite the qubit and add a photon to the cavity depending on its state. Supplemented by an unconditional qubit reset, this gate is suitable for single photon error correction.

Keywords: circuit QED, superconducting circuits, 3D cavity, bosonic codes, qubit, continuous variable, GKP-state, cubic phase state.

Acknowledgements

First and foremost I would like to thank my supervisor prof. Per Delsing. It was my great wish to do research on quantum computers ever since my bachelor and you made that wish come true. Thank you for letting me explore where my curiosity took me and for always being so focused when trying to help me solve the problems I encountered.

I would like to thank all the people who co-authored publications with me. It is a team effort and I would have never made it to this point without you.

I would like to thank all my colleagues from QT, AQP, and QDP. You made MC2 a great place to work. I hope I gave back to you at least a fraction of what you taught me.

I would like to thank my parents and my sister for supporting me in my adventures. Your love and support mean the world to me.

And last but not least, to Edo, my love, thank you for everything.

Marina Kudra, Göteborg, December 2022

List of appended papers

This thesis is based on the work contained in the following papers:

I **Decoherence benchmarking of superconducting qubits**
Jonathan J Burnett, Andreas Bengtsson, Marco Scigliuzzo, David Niepce,**Marina Kudra**, Per Delsing, Jonas Bylander
npj Quantum Information, 5, 54 (2019)

II **Stability of superconducting resonators: Motional narrowing and the role of Landau-Zener driving of two-level defects**
David Niepce, Jonathan J Burnett, **Marina Kudra**, Jared H. Cole, Jonas Bylander
Science advances, 7(39), eabh0462, (2021).

III **High quality three-dimensional aluminum microwave cavities**
Marina Kudra, Janka Biznárová, Anita Fadavi Roudsari, Jonathan J. Burnett, David Niepce, Simone Gasparinetti, Björn Wickman, Per Delsing
Applied Physics Letters, 117, 070601 (2020).

IV **Robust preparation of Wigner-negative states with optimized SNAP-displacement sequences**
Marina Kudra, Mikael Kervinen, Ingrid Strandberg, Shahnawaz Ahmed, Marco Scigliuzzo, Amr Osman, Daniel Pérez Lozano, Mats O. Tholén, Riccardo Borgani, David B. Haviland, Giulia Ferrini, Jonas Bylander, Anton Frisk Kockum, Fernando Quijandría, Per Delsing, Simone Gasparinetti
PRX Quantum, 3, 030301, (2022).

V **Coherent-state quantum process tomography of continuous-variable gates**
Mikael Kervinen, **Marina Kudra**, Shahnawaz Ahmed, Axel M. Eriksson, Fernando Quijandría, Anton Frisk Kockum, Per Delsing, Simone Gasparinetti
To be submitted (2022).

VI **Experimental realization of deterministic and selective photon addition in a bosonic mode assisted by an ancillary qubit**
Marina Kudra, Tahereh Abad, Mikael Kervinen, Axel M. Eriksson, Fernando Quijandría, Per Delsing, Simone Gasparinetti
Submitted to Quantum Science and Technology (2022).

VII **Measurement and control of a superconducting quantum processor with a fully-integrated radio-frequency system on a chip**
Mats O. Tholén, Riccardo Borgani, Giuseppe Ruggero Di Carlo, Andreas Bengtsson, Christian Križan, **Marina Kudra**, Giovanna Tancredi, Jonas Bylander, Per Delsing, Simone Gasparinetti, David B. Haviland
Review of Scientific Instruments, 93, 104711 (2022).

Papers which are outside the scope of the thesis:

I **Three-wave mixing traveling-wave parametric amplifier with periodic variation of the circuit parameters**
Anita Fadavi Roudsari, Daryoush Shiri, Hampus Renberg Nilsson, Giovanna Tancredi, Amr Osman, Ida-Maria Svensson, **Marina Kudra**, Marcus Rommel, Jonas Bylander, Vitaly Shumeiko, Per Delsing
arXiv:2209.07551, (2022).

Contents

CHAPTER 1

Introduction

The first quantum revolution is based on the discrete nature of physical quantities, such as energy states in atoms. The devices that led to the 20th-century technological revolution, use the discreet nature of physics, but they use the collective behavior of many quantum particles together. Most notably, devices that transformed our society are the transistor, the laser, and the atomic clock. They enabled, among other things, computers, the internet, and the global positioning system (GPS). It is fair to say that today's life is hard to imagine without these necessities.

The second quantum revolution is here. We call it a revolution because we expect that the technologies and devices developed will significantly transform our society. The technological leap we made enables us to control individual quantum degrees of freedom instead of the collective ones. Examples of single quantum degrees of freedom we can control are the spins of electrons, the polarization of photons, the excitation states of atoms, etc. The second quantum revolution promises quantum limited sensing, communication with security guaranteed by the laws of physics, efficient simulation of quantum systems using the well-controlled quantum systems, and computations that are beyond the reach of classical computers - quantum computation. Quantum computers are systems

comprised of interconnected qubits, the basic building block of a quantum computer. Qubits can be realized in many different systems e.g. in trapped ions [1], single photons [2] at optical/telecom frequencies, spins of electrons in solid-state devices [3, 4], rare-earth ions in solid-state crystals [5], superconducting circuits [6], etc. One of the most promising platforms is superconducting circuits or circuit quantum electrodynamics (cQED) [7, 8]. Multiple working systems with over 50 qubits have been demonstrated [9, 10, 11]. Whichever physical system we choose to encode our quantum information in, it is going to be susceptible to different sources of errors. For quantum computers to perform advanced and useful computations [12, 13] we need to track and correct these errors, by performing so-called quantum error correction [14, 15, 16]. We need to redundantly encode one logical qubit into multiple physical qubits. Each qubit has to have its physical error rate below a certain threshold for that specific error-correcting protocol. The further below this threshold the error rate is, the lower the number of physical qubits we will need to form the logical qubit. This is important as it reduces the number of hardware components and the complexity of the system.

Mainstream architectures are built on discrete variable qubits arranged in some lattice. In this thesis, we will describe so-called bosonic qubits [17, 18, 19] that reside in harmonic oscillators (resonators). Such qubits take advantage of the many available quantum levels to redundantly encode a binary qubit. However, universal control of a bosonic qubit requires the presence of nonlinearity. We accomplish this requirement by coupling the bosonic mode to an ancilla transmon qubit. If the resonator is a 3D cavity [20, 21, 22], as is the case for many research groups pursuing this path, the physical lifetime of the bosonic qubit is about 10 times higher than that of planar two-level qubits. The first layer of quantum error protection can be encoded in one resonator instead of many two-level systems, making it hardware efficient. We can pick a particular qubit encoding, for example Scrödinger cat states [23, 24, 25], Binomial encoding [26, 27, 28] or Gottesman-Kitaev-Preskill (GKP) [29, 30, 31, 32] encoding. Applying an error correction protocol we can then extend the lifetime of the physical mode. Furthermore, for bosonic systems, there is one dominating source of error, namely the single-photon loss that should be corrected. Adding this additional layer of error protection

plus the longer lifetimes means we need fewer bosonic qubits to form a logical qubit.

Currently, the limiting factor for the bosonic qubits seems to be the ancilla qubit. It is typically the component with the worst coherence, but it is necessary as it introduces the nonlinearity needed to control the harmonic mode. Furthermore, demonstrating larger connected bosonic systems remains a practical challenge.

Succinctly, the reason why you would consider building a bosonic microwave qubit, as the title of this thesis indicates, is that it is a small system, that is reproducible, robust, and interesting from both engineering and scientific perspectives. The system Hamiltonian is as simple as they come, but the interesting and useful physics comes from the many ways we can drive the system [33].

1.1 Outline of the thesis

This thesis provides an overview and the background for the work presented in the appended papers. It can be interpreted as an instruction guide on creating a bosonic microwave qubit. The guide starts with building hardware components and ends with a suggestion on the implementation of a single photon quantum error correction layer. Each chapter first lists the theory needed to understand the results of the papers summarized in that chapter.

Chapter 2 introduces the cryogenic setup and the state-of-the-art room-temperature hardware that generates the microwave pulses that we need to perform all of the experiments in this thesis. Paper VII describes the latest generation of room-temperature measurement and control system we used, applied to a discrete variable two-qubit system.

Chapter 3 and papers I-III deal with the hardware components that are needed, namely a superconducting transmon qubit and a 3D superconducting cavity. This chapter deals with coherence properties and it is trying to establish the sources of noise that limit those properties. Paper III provides a blueprint for reproducibly fabricating high-quality aluminum 3D stub-geometry cavities. Cavities have quality factors close

to 100 million after etching and annealing.

Chapter 4 and papers IV-V deal with initialization, control, and characterization of the bosonic states in the resonator. In paper IV, we create arbitrary bosonic states using an interleaved sequence of displacement and optimized SNAP gates. In paper V, we use the same sequence of gates to implement a bosonic X-gate on a binomially encoded qubit and use coherent state process tomography to characterize it.

Chapter 5 and paper VI introduce the off-resonant driving of the qubit-cavity system. In particular, we implement a two-excitation transition that selectively adds a photon to the cavity mode and excites the qubit depending on the state of the cavity. We name this gate selective number-dependent arbitrary phase photon addition (SNAPPA). In paper VI, we show how to calibrate the comb of off-resonant drives used to implement the SNAPPA gate. We envision that by encoding a logical qubit in a superposition of a four-component cat state and applying SNAPPA gate followed by an unconditional qubit reset, we can successfully protect the logical qubit from the single-photon loss.

CHAPTER 2

Experimental setup

2.1 Cryogenic setup

All our experiments are performed in a dilution refrigerator. The samples are mounted to the mixing chamber and cooled down to below 10 mK. The signals from the room-temperature equipment are attenuated at each temperature stage to suppress noise from the electronics and room-temperature noise. They are then directed through a set of circulators or isolators that isolate the noise coming from the output chain and separate the input and output signals in the case of reflection measurements. After interacting with the sample, the signals are passed through superconducting coaxial cables, in order to minimize the losses, to either a traveling wave parametric amplifier (TWPA)[1], when available, or straight to a high electron mobility transistor (HEMT) amplifier. Signals are further amplified at room temperature and then digitized. The room-temperature electronics is described in Sec. 2.3.

Wiring diagrams are similar for all experiments, up to how many input and output lines they use and whether the measurements are performed in reflection or in a notch configuration. As an example, a wiring diagram

[1]We acknowledge IARPA and Lincoln Labs for providing the TWPA used in our experiments

from papers IV and V is given in Fig. 2.1. In paper VI the only difference is the absence of the TWPA amplifier.

The cavity drive port (drive line in Fig. 2.1) is under-coupled to enable the best lifetime of the cavity, while the readout resonator drive port (drive line reflection in Fig. 2.1) is over-coupled to enable fast readout of the qubit state. The same line is used to send pulses to the qubit.

It is important to use filtering and shielding to prevent infrared (IR) photons from reaching the superconducting parts of our devices. They have energies larger than the superconducting gap and would therefore create quasiparticles and resistive loss. Furthermore, it is important to minimize the magnetic field fluctuations. This is why all our samples are placed in a light-tight copper shield that is surrounded by a mu-metal shield. An additional mu-metal shield is placed at room temperature. The mixing chamber can is coated by superconducting tin to further improve magnetic shielding. Homemade ecosorb filters were mounted on the input lines for the measurements in papers I and II to prevent IR photons from reaching the samples via the input line. It would have been good to have these filters for all the other experiments too.

2.2 Sample fabrication

All the chips were fabricated in Chalmers Myfab cleanroom. In papers I, II and VII the superconducting circuits are coplanar. They are made out of aluminum patterned on the silicon substrate. In papers IV-VI the circuits are instead stripline (i.e. no ground plain on the chip). The superconductor is still aluminum, but the substrate is either silicon or sapphire. I designed the stripline chips, but did not fabricate any of the chips myself. They were fabricated by A. Bengtsson and J. Burnett in papers I, II and VII, D. Niepce in paper II, A. Osman and D. Pérez Lozano in paper IV and M. Kervinen in papers V and VI. The fabrication recipe for aluminum on silicon chips can be found in the Ph.D. thesis by M. Scigliuzzo [34]. The fabrication recipe for NbN nanowires used in paper II can be found in the Ph.D. thesis by D. Niepce [35].

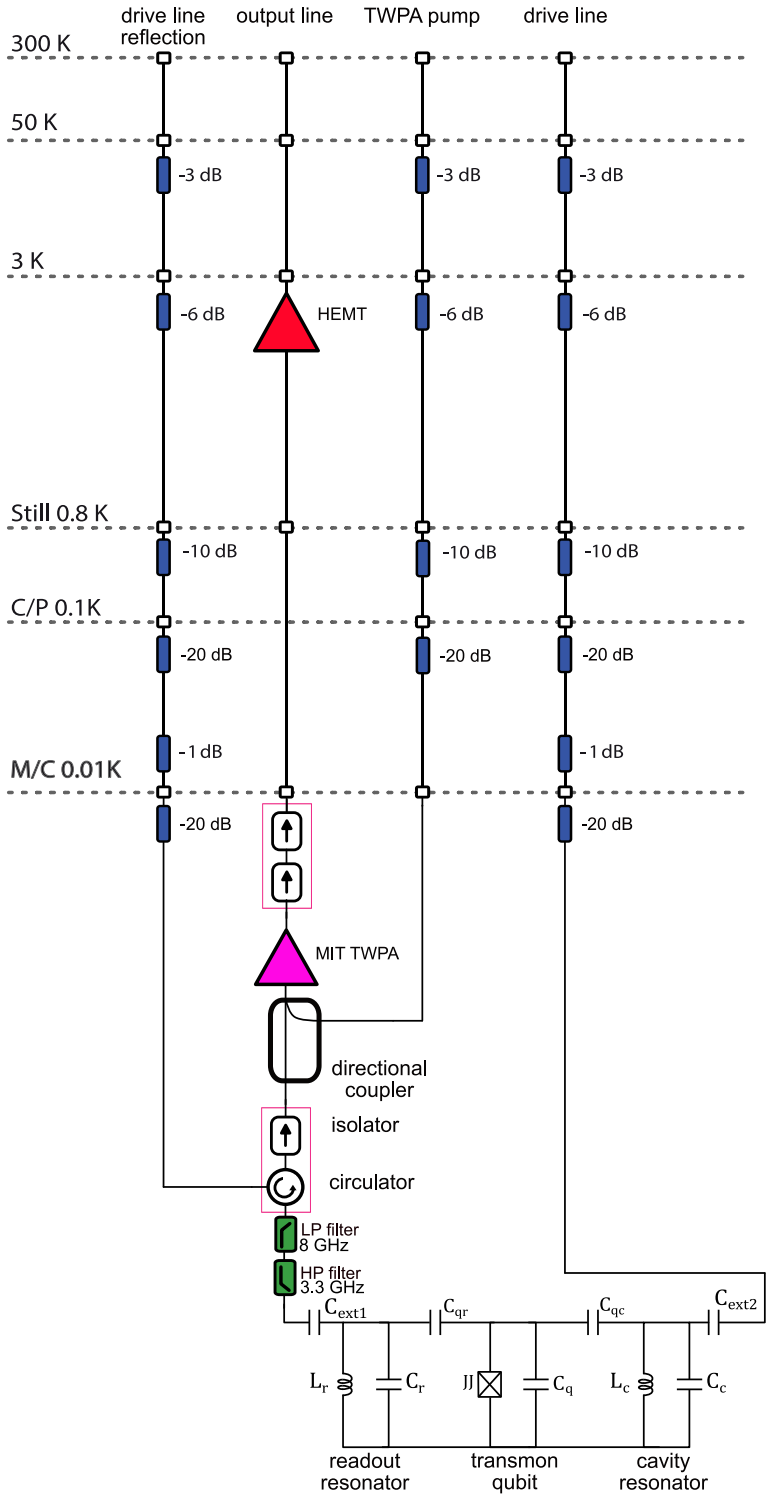

Figure 2.1: Example of the wiring diagram in the dilution refrigerator. The device being measured is represented as a circuit model. This is the wiring diagram used in papers IV and V. In paper VI the only difference is the absence of the TWPA amplifier.

2.3 Room temperature electronics

There are two main types of measurements we perform.

i) The continuous wave or spectroscopic measurements are measurements where we send a long tone of defined frequency and then sweep this frequency. We are interested in the frequency response of, for example, a 3D cavity (papers II and III) or a readout resonator (all the other appended papers). We can find the resonance frequencies and quality factors of these modes, and it is usually the first measurement we do when we start measuring a device. We usually perform this measurement using a vector network analyzer (VNA), and after we are done, we have to rewire our cables to prepare for the time domain measurements.

ii) Time domain measurements allow us to perform all the experiments described in papers I and III-VII. All these experiments can be summed up in the following way: first, we shape the pulses that have a carrier frequency of a few hundred MHz, and then we schedule when these pulses should be output and on which channels. We upconvert the pulses to the appropriate frequencies (usually between 4-8 GHz), and send them through the cryostat. Some of the pulses, namely the ones sent to the readout resonator, get reflected from the sample, amplified, downconverted to a few hundred MHz, and then digitized. The digitized signal is usually processed by further down-converting it to DC and integrating it, so the outcome of one such measurement is usually a complex number representing the quadratures or the amplitude and the phase of the readout pulse. Based on this one complex number, we can distinguish whether the qubit is in the ground state or the excited state and this is the backbone of our qubit measurement procedure.

Most devices that perform time domain measurements can only produce pulses with a frequency of a few hundred MHz. These pulses are then up- and down-converted with analog mixers and separate local oscillator (LO) sources. This presents several problems. Analog mixers are not ideal, they suffer from LO leakage and non-perfect image rejection and they require calibration by using yet another instrument, e.g. a spectrum analyzer. Separate LO sources are hard to sync with the in-

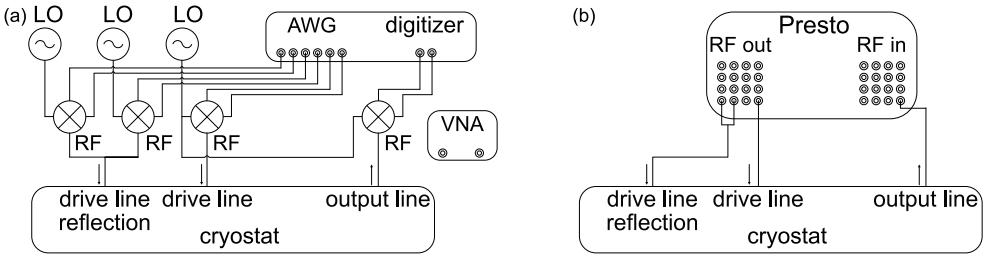

Figure 2.2: Room temperature measurement equipment. (a) The setup used in papers I-V. (b) Presto substitutes all of the instruments in (a) and performs digital up- and down-conversion. It was used in papers VI-VII.

struments producing the pulses, meaning experiments such as two-qubit gates are tricky to perform. We helped develop an instrument called Presto (paper VII) that solves a lot of the beforementioned problems and has some added benefits. The details of the architecture of the instrument and a use case, where two coupled qubits were characterized, is given in paper VII. I used this instrument in paper VI and its predecessor (called Vivace) for measurements in papers IV and V. Here, I will go through the features I find the most useful.

Presto can do both continuous wave and pulsed measurements, so once the cables are connected, there is no need to re-arrange them.

The most convenient feature of Presto is that it does digital up- and down-conversion. This means perfect mixing, without any LO leakage and output is only one sideband and no mixer calibrations. This saves time and is very important when driving multiple off-resonant transitions (paper VI). All the off-resonant pulses induce Stark shifts to both the qubit and the cavity and having extra tones due to mixer imperfections could further complicate the calibration of these pulses (see paper VI and Cha. 5 for more details). Digital up- and down-conversion also means that digital local oscillators that are created on the same chip are always synchronized. This is important when performing a two-qubit gate such as an iSWAP (see paper VII).

It is possible to do a real-time template matching with low latency (see paper VII). I used template matching for signal down-conversion and integration. This enables us to collect single-shot measurement data

without transferring GBs of data to the PC. For me, this was useful when tuning the readout pulses. Low latency will be crucial for implementing an active qubit reset which is one option to supplement SNAPPA gates to do quantum error correction (the outlook of paper VI). In paper VII we performed an active reset of the qubit to cool-down the qubit from the initial excited state population of 5.8% down to 0.7%. Template matching and the low latency of Presto are key features that enable this.

Finally, it is possible to output long sequences of pulses and to sweep multiple parameters of those pulses with just one call of the instrument. This was useful for acquiring Wigner tomography, where each pixel in the image was measured sequentially starting from the bottom left corner of the image, and ending in the top right corner. Then, the whole picture was measured as many times as we wanted to average, and the averaging was done interleaved, all in one call to the instrument. In paper VII we use this property to perform single-qubit-gate-interleaved benchmarking.

CHAPTER 3

Resonators and transmon qubits

Quantum information is fragile. Our goal is to keep the quantum states "alive", i.e. stay coherent, for as long as possible. We encode the quantum information in a physical system such as a transmon qubit or a 3D superconducting resonator, but there are always unwanted interactions with the environment that cause the loss of "quantumness" i.e. decoherence. "Quantumness" is measured by coherence properties. We can represent the state of any quantum system with a density matrix $\rho(t)$. Diagonal elements of the density matrix represent populations of the basis states, and off-diagonal elements represent coherences between these states. There are two main decoherence channels. The loss of population is described by the relaxation time T_1 or equivalently by a quality factor Q. The loss of off-diagonal elements is described by dephasing time T_φ. The total decoherence time T_2 is $1/T_2 = 1/(2T_1) + 1/T_\varphi$.

In this chapter, we discuss how we can measure coherence parameters, how we can discern what limits them, and what we can do to extend the lifetime of quantum information. We revisit the main results from Papers I-III.

3.1 Quality factor

The figure of merit we use to compare resonators is the internal quality factor. The total or loaded quality factor describes how many oscillations it takes before the energy stored in the resonator is dissipated [36]:

$$Q_l = 2\pi \frac{E_{total}}{E_{lost\ per\ cycle}}. \tag{3.1}$$

The inverse of the loaded quality factor is the sum of the inverse of the internal and the external quality factor:

$$\frac{1}{Q_l} = \frac{1}{Q_{int}} + \frac{1}{Q_{ext}}. \tag{3.2}$$

The external quality factor is something we can easily design by, for example, choosing the length of the coupling pin in 3D cavities or designing the distance between the resonator and the transmission line in coplanar circuits. Depending on the use of the resonator, we are interested in different limits. If we are interested in measuring the internal quality factor, it is best to be as close to critically coupled as possible i.e. $Q_{ext} = Q_{int}$. This way, the resonator's frequency response in both amplitude and phase is substantial, which results in a more confident fit, especially at low powers. However, if we instead want to use the resonator as a long-lived storage mode, we want our system to be undercoupled i.e. $Q_{ext} \gg Q_{int}$. In this regime, the lifetime of the photon inside the resonator will be limited by the internal quality factor and the rate at which it leaks out into the transmission line will be negligible. If we want to readout the state of the qubit dispersively coupled to a resonator, we want the resonator to be over-coupled $Q_{ext} \ll Q_{int}$. In this case, we want to collect as much information about the state of the resonator, as fast as possible, so the rate of the photons leaking out should be large. There is, of course, a limit on how small Q_{ext} can be without compromising the lifetime of the coupled qubit. This is determined by the Purcell effect [37].

We measure the quality factor by performing a simple reflection measurement using a vector network analyzer (VNA). We fit the complex

response to a so-called circle-fit [38]:

$$S_{11} = ae^{i\alpha}e^{-i2\pi f\tau}\left(\frac{2Q_l/Q_{ext}e^{i\phi}}{1+2iQ_l(f/f_r-1)}-1\right), \tag{3.3}$$

here S_{11} is the reflection coefficient, Q_l and Q_{ext} are the loaded and external quality factors, respectively. The internal quality factor is extracted from $1/Q_{int} = 1/Q_l - 1/Q_c$. f_r is the resonance frequency. ϕ accounts for the impedance mismatch between the resonator and the transmission line. There are also measurement setup parameters a, α, and τ, where a is the background offset accounting for net attenuation of the signal sent from the VNA, α is a global phase offset and τ is an electrical delay in our lines.

When measuring qubits it is much more common to measure relaxation time T_1. Relaxation time is frequency dependent, so if we are interested in comparing qubits at different frequencies we can convert it into a quality factor:

$$Q = 2\pi f_q T_1, \tag{3.4}$$

where f_q is the qubit frequency.

3.2 Sources of decoherence

The internal quality factor is determined by a combination of loss channels Q_i:

$$\frac{1}{Q_{int}} = \sum_i \frac{1}{Q_i}. \tag{3.5}$$

From the equation, we can see that it is typically limited by the dominant source of loss. To further distinguish the geometry participation from material properties we can rewrite Eq. 3.5 by using participation ratios [39]:

$$\frac{1}{Q_{int}} = \sum_i \frac{1}{p_i \tan\delta_i}, \tag{3.6}$$

here $\tan\delta_i$ is the material loss tangent and p_i is the participation ratio that depends only on the geometric distribution of mode fields.

$$p_i = \frac{Energy\ stored\ in\ volume(i)}{Total\ energy}. \tag{3.7}$$

Examples of sources of decoherence include coupling to a bath of two-level systems, quasiparticles, seam losses, radiation losses, etc. To distinguish between the different contributions, we can examine the functional dependence of resonant frequency and quality factor with temperature, power, and geometry parameters.

3.2.1 Two-level system (TLS) loss

Two-level systems (TLSs) are unwanted defects that are often found on surfaces, interfaces, or in the bulk of amorphous dielectrics. Superconducting resonators couple to the ensemble of dipoles in a narrow spectral range close to the resonant frequency. In low-temperature, low-power regime, two-level systems are in their ground state and can absorb microwave photons [40] and limit the quality factor. These TLSs can be saturated either by increasing microwave power or by increasing the temperature [41]. The standard TLS model captures both temperature and power dependence of the internal quality factor [42, 43, 44]:

$$1/Q_{TLS} = F\delta_{TLS} \tanh\left(\frac{hf_r}{2kT}\right)(1 + n/n_c)^{-\beta}, \tag{3.8}$$

where n is the average number of photons, n_c is the critical photon number needed to saturate a TLS and β is a phenomenological constant. F or p_{diel} is the participation ratio and δ_{TLS} is the loss-tangent. The first parameter we extract from the fit is the product of the participation ratio of the electric field (F) and the two-level system loss tangent (δ_{TLS}).

Participation ratios have been derived in [21], and for the dielectric loss it is:

$$p_{diel} = \frac{\int_{\text{diel}} \epsilon |\vec{E}|^2 dV}{\int_{\text{tot}} \epsilon |\vec{E}|^2 dV}. \tag{3.9}$$

If the surface oxide is thin we can approximate:

$$p_{diel} \approx \frac{t_{ox} \int_{\text{surf}} |\vec{E}_{vol}|^2 dS}{\epsilon_{r,ox} \int_{\text{tot}} |\vec{E}_{vol}|^2 dV}, \tag{3.10}$$

3.2.2 Quasiparticle loss

Resistive loss in superconductors at non-zero frequencies stems from quasiparticles. The source of equilibrium quasiparticles is finite temper-

ature. The concentration of quasiparticles is highly temperature dependent. The resonance frequency shift and quality factor degradation due to temperature dependent quasiparticle concentration is described by the Mattes-Bardeen equations [45, 46]. Often, the concentration of quasiparticles cannot be explained by equilibrium concentration. Sources of non-equilibrium quasiparticles are photons that have higher energy than the superconducting gap (e.g. infra-red photons) or ionizing radiation [47, 48] that hit the superconductor and cause Cooper-pair breaking.

The participation ratio of the resistive loss is given by

$$p_{res} = \frac{\lambda \int_{\text{surf}} |\vec{H}|^2 dS}{\int_{\text{tot}} |\vec{H}|^2 dV}, \tag{3.11}$$

here λ is the skin depth that represents the exponential decay of the magnetic field into the conductor. The quality factor due to resistive (quasiparticle) losses is given by

$$Q_{res} = \frac{\omega \mu_0 \lambda}{R_\square} \frac{\int_{\text{tot}} |\vec{H}|^2 dV}{\lambda \int_{\text{surf}} |\vec{H}|^2 dS}, \tag{3.12}$$

where ω is the angular resonance frequency, μ_0 is the permeability of vacuum, $R_\square$ is the quasiparticle induced temperature dependent sheet resistance and $\vec{H}$ is the magnetic field strength.

3.2.3 Seam loss

Seam loss is present whenever we have a current flowing over two pieces of metal that do not have perfect contact which is typical in 3D cavities. The quality factor associated with this loss mechanism can be expressed as [21]:

$$Q_{seam} = g \frac{\omega \mu_0 \int_{\text{tot}} |\vec{H}|^2 dV}{\int_{\text{contour}} |\vec{H}_{||}|^2 dl}, \tag{3.13}$$

where $g = G/L$ is the constant conductance per unit length along the seam. We can conclude that it is a good idea to make low-loss seams (for example welding two pieces together) or to place seams where the magnetic field is low, to maximize this quality factor.

3.2.4 Radiation loss

Radiation loss is associated with the energy of the mode being radiated into free space, precisely what antennas are made for. This is a fairly uncommon setup in our experiments as we almost always have a package around our chip, or in the case of 3D cavities, we have closed pieces. Radiation loss is highly geometry dependent and in general, does not have a simple analytical expression. We don't want to expose our quantum modes to holes through which they can radiate out because those same holes would expose them to infrared radiation that could increase the quasiparticle loss.

3.3 Geometry

The main reason to store a bosonic mode in a 3D cavity rather than in a planar circuit is that it is easier to get better quality factors and equivalently longer lifetimes. In aluminum 3D cavities, it is "usual" to get lifetimes of around 1 ms [20], with some niobium cavities reaching 2 s [22]. For planar circuits it is "usual" to get around 100 μs [49, 50].

There are several factors to consider when choosing the shape of a 3D cavity. One should make sure all seams are in areas of low magnetic field. This includes the seams we will create when inserting the qubit chip(s). Rectangular cavities for example were shown to be limited by seam loss [21]. Next, the distribution of the fields should be considered. Modes that have the maximums of their fields in the vacuum will in general have higher quality factors. Coupled with bigger mode volumes, this is what makes cylindrical and accelerator-shaped cavities have quality factors exceeding 10^9 [51, 22]. Big mode volume also makes it so that the coupling to a qubit in these geometries is challenging, and to our knowledge, it has not been realized to date without seriously compromising the quality factor of the cavity.

This leaves us with a stub geometry cavity [20]. It can be thought of as a $\lambda/4$ resonator formed by a stub at the bottom of the cavity connected with a cylindrical wave-guide on top (Fig. 3.1(a)). The cut-off frequency of the cylindrical wave-guide is below the resonance frequency of the fundamental mode, so both the electric and the magnetic fields

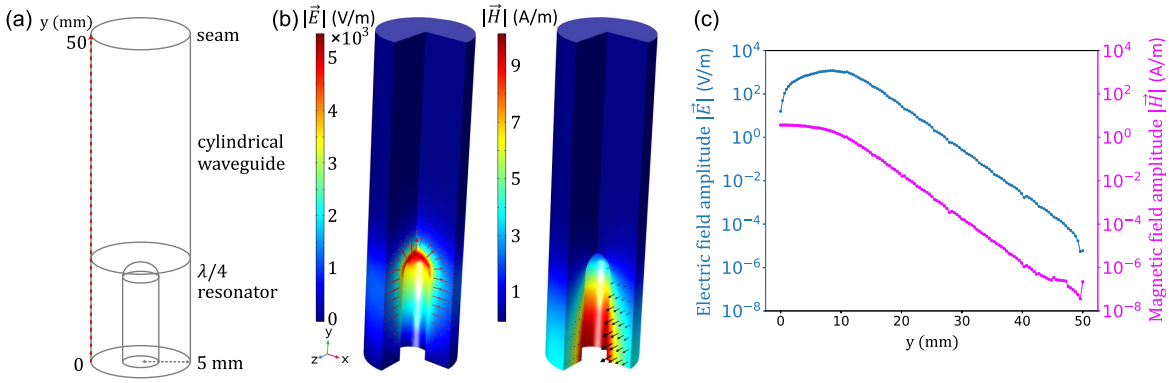

Figure 3.1: (a) Wire frame sketch of the stub geometry cavity. The radius of the mode volume is 5 mm and the height is 50 mm. (b) In color scale amplitude of electric (left) and magnetic (right) field in a stub geometry 3D cavity. The vector directions are indicated by arrows. The fields were simulated using an eigenmode solver in COMSOL. (c) Line cuts of electric (blue) and magnetic (magenta) field magnitudes along the y-axis depicted as black dashed line in (a). Both electric and magnetic fields decay exponentially towards the top of the cavity where the seam is placed.

get exponentially suppressed in the wave-guide (Fig. 3.1(c)). The field distribution is depicted in Fig. 3.1(b). Both the electric and magnetic fields are concentrated around the stub. A good feature of this geometry is that the seam loss can be made arbitrarily small by extending the cylindrical part of the cavity. Also, the mode volume is small, so coupling to the qubit with coupling strength of $g = 100\,\mathrm{MHz}$ is easily achievable. The downside is that the maxima of the fields occurs at the surface of the metal. This will make the participation ratios for both dielectric and quasiparticle losses higher compared to the modes whose maxima are in vacuum.

3.4 Analyzing fluctuations of parameters in time

We can learn a lot from analyzing the fluctuations of different parameters in time. By using frequency and time domain analysis we can recognize the features of different sources of noise. In paper I we analyze the fluctuations of relaxation times of two qubits over several months, and in paper II we carefully follow the resonant frequencies of three different kinds of resonators. We analyze the fluctuations of parameters both in the time domain and in the frequency domain.

3.4.1 Frequency domain analysis: Power spectral density

Any physical signal can be decomposed into several discrete frequencies according to Fourier analysis. Power spectral density (PSD) is calculated by taking the Fourier transform of the signal's autocorrelation function [52, 35]:

$$S_y = 2\int_0^\infty \langle y(t)y(t+\tau)\rangle e^{-i\omega\tau}d\tau, \tag{3.14}$$

There are several limitations to using PSD to analyze noise fluctuations. Averaging the signal does not always improve the signal-to-noise ratio, discrete sampling of the signal means aliasing and spectral leakage, and frequency drifts are not captured. Therefore, we use the Allan variance, described in the following chapter, in conjunction with PSD when analyzing our data.

Most noise sources can be modeled as a sum of noise processes with a spectral density of the form $S_y(f) \propto f^\alpha$. These processes are known as power-law noise. A TLSs power spectrum, on the other hand, is described by a Lorentzian function:

$$S_y(f) = \frac{4A^2\tau_0}{1+(2\pi f\tau_0)^2}, \tag{3.15}$$

with characteristic switching time τ_0 and amplitude A.

3.4.2 Time domain analysis: Allan variance

Allan variance, also known as two-sample variance, is a measure of frequency stability and is given by [53]:

$$\sigma_y^2(\tau = n\tau_s) = \frac{1}{2(M-1)}\sum_{i=1}^{M-1}(\bar{y}_{i+1}-\bar{y}_i)^2 \tag{3.16}$$

Here, $\bar{y}_i$ is the i-th mean fractional frequency of a total number M over the measurement interval $n\tau_s$, where τ_s is the sampling interval. The fractional frequency is a measure of the deviation of the signal from the reference $\bar{y}_i = (f_i - f_r)/f_r$, where f_i is the i-th measured frequency and f_r is the reference frequency. Overlapping Allan variance [54] is an

improvement on the Allan variance. It uses all the possible combinations of the data set:

$$\sigma_y^2(\tau = m\tau_s) = \frac{1}{2m^2(M-2m+1)} \sum_{j=1}^{M-2m+1} \left[\sum_{i=j}^{j+m-1} (\bar{y}_{i+1} - \bar{y}_i) \right]^2 \quad (3.17)$$

A Lorentzian noise process has the following form in the Allan deviation [55]:

$$\sigma_y^2(\tau) = \frac{A\tau_0}{\tau} \left(4e^{-\tau/\tau_0} - e^{-2\tau/\tau_0} + 2\frac{\tau}{\tau_0} - 3 \right)^{1/2} \quad (3.18)$$

with the same two parameters as in the PSD, i.e. the characteristic switching time τ_0 and the amplitude A.

3.5 Qubit decoherence statistics (Results summary)

In paper I we study the decoherence parameters of two fixed frequency transmon qubits over several days and several cooldowns gathering significant statistics. Transmon qubits are placed in two separate sample boxes and their relaxation time T_1 and Ramsey decay time T_2^* are measured repeatedly. These parameters fluctuate and their statistics are captured well by fitting a Gaussian distribution. Average relaxation times and their standard deviation over about 65 hours are $\langle T_{1A} \rangle = 44\,\mu$s, $\sigma_A = 8\,\mu$s for qubit A and $\langle T_{1B} \rangle = 72\,\mu$s, $\sigma_B = 13\,\mu$s for qubit B (Fig. 3.2(a) and (b)). We found that the fluctuations are not correlated, meaning that local sources of noise are dominating.

When repeatedly measuring T_1 of qubit A, 3% of the time we observe jumps in relaxation time between two discreet values (Fig. 3.2(d)). We observe these jumps because we do not interleave the averaging of each trace. In 5% of the traces, we see revivals instead of a simple exponential decay (Fig. 3.2(e)). We interpret this as a single TLS frequency fluctuating and 5% of the time resonantly exchanging energy with the transmon qubit. From the oscillations, we can extract the coupling rate with the TLS to be $g = 4.8\,$kHz.

From the statistical analysis of T_1 times (using Allan deviation and spectral density) we conclude that a few Lorentzians and a white noise

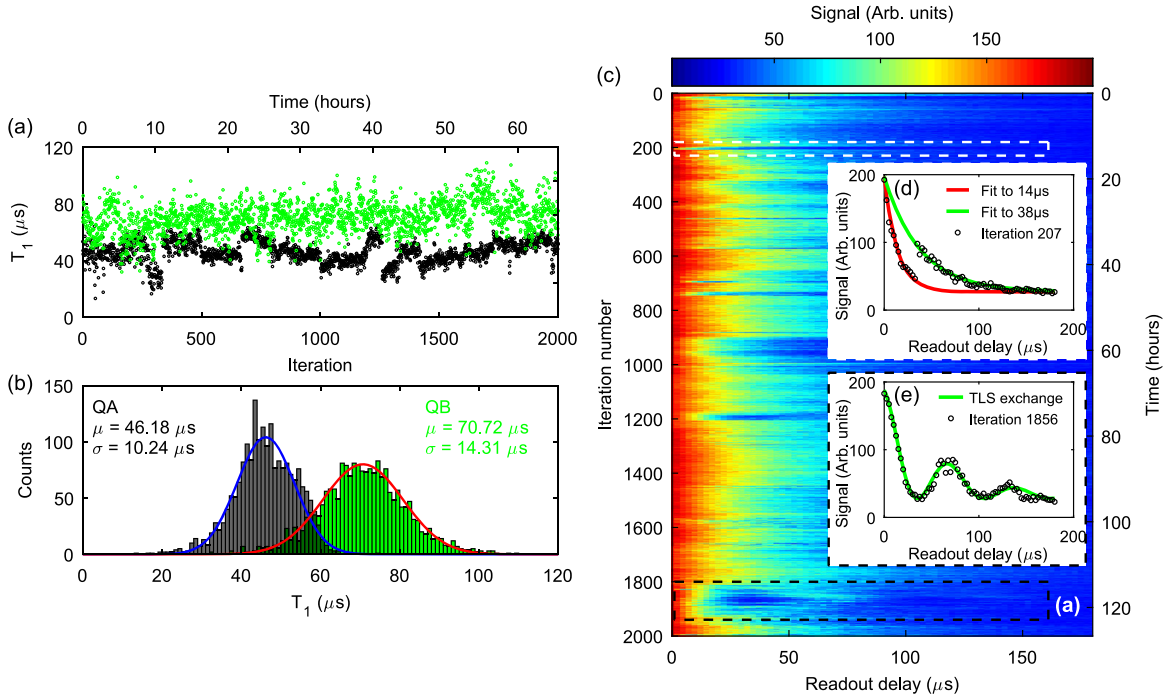

Figure 3.2: Adapted from paper I. (a) Repeated simultaneous measurements of the relaxation time of two qubits, qubit A in black and qubit B in green. 2000 consecutive measurements that lasted approximately 65 hours are presented. (b) Histograms of the relaxation times in (a) fitted to Gaussian distributions. (c) Raw data of relaxation times of qubit A. (d) In about 3% of data traces the relaxation time changes within a single trace. (e) In approximately 5% of all traces, the decay is not purely exponential. The appearance of revivals is due to the resonant exchange of energy with a single TLS.

floor fit well the data sets we collected over many hours and several cooldowns. The switching rates are found to be between 71 μHz and 1.9 mHz. These switching rates are in a good agreement with the switching rates found in other TLS studies [44, 56, 57], and are six orders of magnitude smaller than the rates associated with quasiparticle recombination in aluminum (1 kHz) [58], or tunneling in transmons (0.1-30 kHz) [59].

Our results point to TLSs being a limiting factor in the temporal stability of transmon qubit coherence parameters.

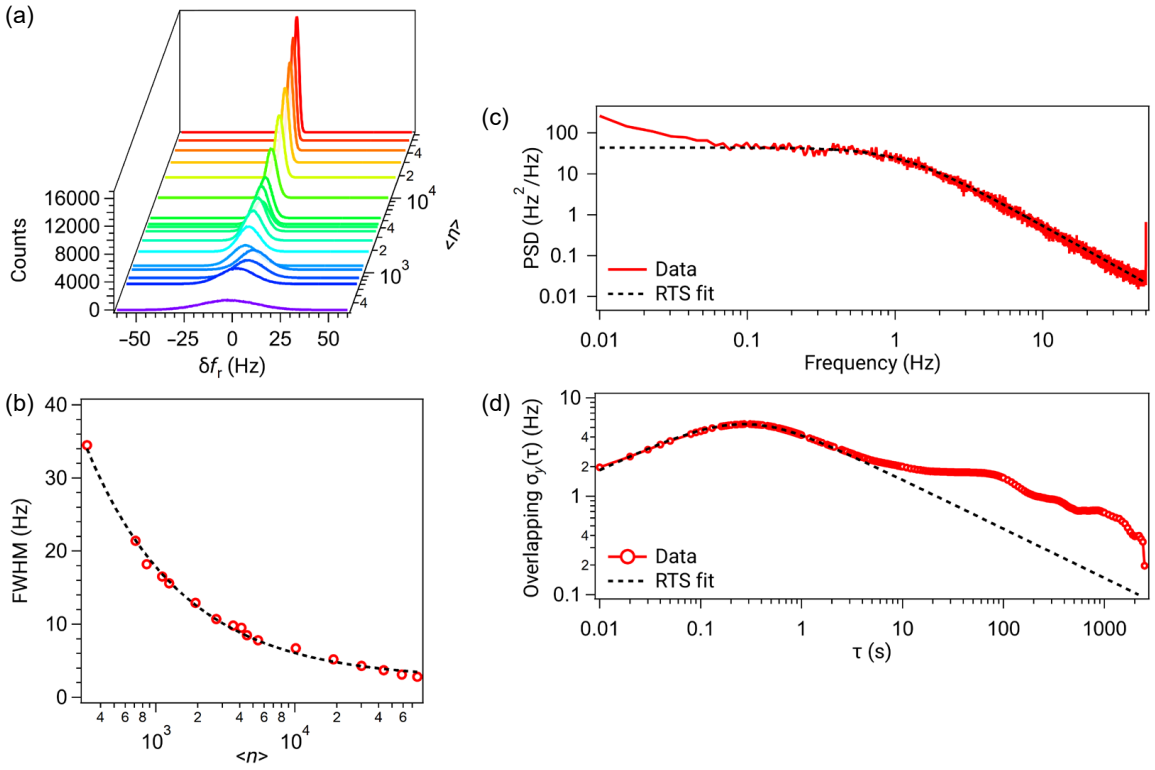

Figure 3.3: Adapted from paper II. All the data is measured on a 3D microwave cavity at a temperature of $T = 10\,\mathrm{mK}$. (a) Histograms of repeated frequency measurements at different powers. (b) The full width at half maximum (FWHM) of the frequency histogram peaks in (a) vs. average photon number fitted to functional form $F_0+F_1/\langle n\rangle^\beta$ with $\beta = 0.63$. Example of (c) Welch power spectral density and (d) overlapping Allan deviation measured for $\langle n\rangle = 715$ photons. Both data in (c) and (d) are fitted to a Lorentzian model using common fitting parameters.

3.6 Resonator resonance frequency fluctuations (Results summary)

In paper II we carefully measure the fluctuations of the resonance frequency of three different resonators: A NbN nanowire, a coplanar aluminum resonator, and a 3D aluminum stub geometry cavity. We do this using a Pound frequency-locked loop (P-FLL). The theory behind the P-FLL measurement and the measurement setup are explained in the Ph.D. thesis by David Niepce [35]. I will focus on the results of the measurement and in particular, the results of the 3D cavity.

The 3D cavity that we measure has an internal quality factor of 11 million at low power. At each power, we measure 10^6 data points at

100 samples/s. Histograms for each power are presented in Fig. 3.3(a). We observe a symmetric peak at each power and the width of the peak decreases with increasing power. The full width at half maximum (FWHM) is fitted to the functional form $F_0 + F_1/\langle n\rangle^\beta$ with $\beta = 0.63$ (Fig. 3.3(b)). The quality factor of a resonator limited by TLS noise also scales with average photon number as $(1 + \langle n\rangle/n_c)^\beta$. β equal to 1/2 is predicted by the standard tunneling model. However, variations from this scaling have been observed [60, 61, 62] and interpreted as TLS-TLS interactions [63, 64, 60]. Indeed, in paper III the β that we fit a power dependence of the TLS model of another 3D cavity is 0.11. And this is the typical value that we see. The power dependence for this particular cavity is presented in paper III Fig. S2(c), and cannot be faithfully fitted to a TLS model due to lack of data at higher power, where we would observe the beginnings of the high power saturation.

Notice that at the highest measured average photon number ($\langle n\rangle = 6 \cdot 10^4$) the FWHM = 2 Hz. The frequency is so stable that its noise is lower than the frequency reference of the signal generator's phase-locked loop. In fact, in paper III Fig. S1(c) we observe a peak around 200 mHz that is a consequence of this fact.

At each power, we compute the Welch power spectral density [65] (PSD) and the overlapping Allan deviation and fit a single dominant Lorentzian using common fitting parameters (see example in Fig. 3.3(c) and (d)). We do this for three different resonators and present all the fitted data in Fig. 3.4. Even though the materials, quality factors, and geometries are very different in the case of three different resonators, the switching times of the TLS that dominates the frequency fluctuation all fit to an empirical power law $\tau_0(\langle n\rangle) = (1s)(\langle n\rangle/n_c)^{-\alpha}$, where $\alpha = 1.1$ for all devices and n_c is a device dependent parameter (Fig. 3.4(b)). The switching rates at close to one average photon are 3 mHz for the coplanar resonator and 0.4 mHz for the 3D cavity. These numbers fit the order of magnitude that we found in paper I for the switching rates of statistical analysis of T_1 fluctuations of aluminum transmon qubits. The amplitudes of the fluctuations are orders of magnitude different, but they follow a $1/\sqrt{n}$ decrease until saturating at some amplitude A_0 (Fig. 3.4(a)). Although the microscopic origin of the TLSs is different

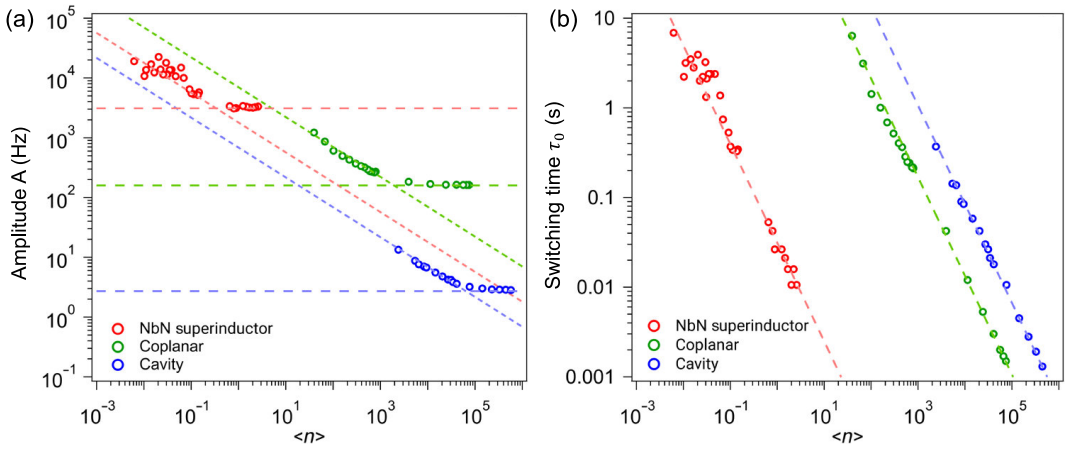

Figure 3.4: Adapted from paper II. Power dependence of the Lorentzian noise (a) amplitude A and (b) switching time τ_0 for the three different resonators. The horizontal dashed lines in (a) indicate the saturation amplitude A_0 related to minimum FWHM in Fig. 3.3(b). Diagonal lines in (a) indicate $1/\sqrt{n}$ scaling and not a fit. The dashed lines in (b) are fits of τ_0 to empirical power law $(\langle n \rangle / n_c)^{-\alpha}$ with $\alpha = 1.1$.

in these resonators, they all share the same power behavior.

The best cavity we produced in paper III has a low-power quality factor of 115 million, 10 times bigger than the one measured in paper II. It would be an interesting experiment to see if the setup we used can at all measure the frequency fluctuations of this cavity since we would expect them to be even smaller and well below the frequency stability of the setup.

Reagor et al. [20] established the contribution of the ancilla qubit, coupled to the 3D cavity, to the degradation of the cavity mode relaxation and dephasing time by studying the quality factor vs. temperature and the qubit steady-state population. The frequency fluctuations could further uncover the type of noise that the cavity mode inherits from the coupled qubit. This would be particularly interesting in the case of a very small dispersive coupling χ around tens of kHz [66], where we would expect the qubit contribution to be diminished, but we see the coherence times of the cavity to be sub-millisecond.

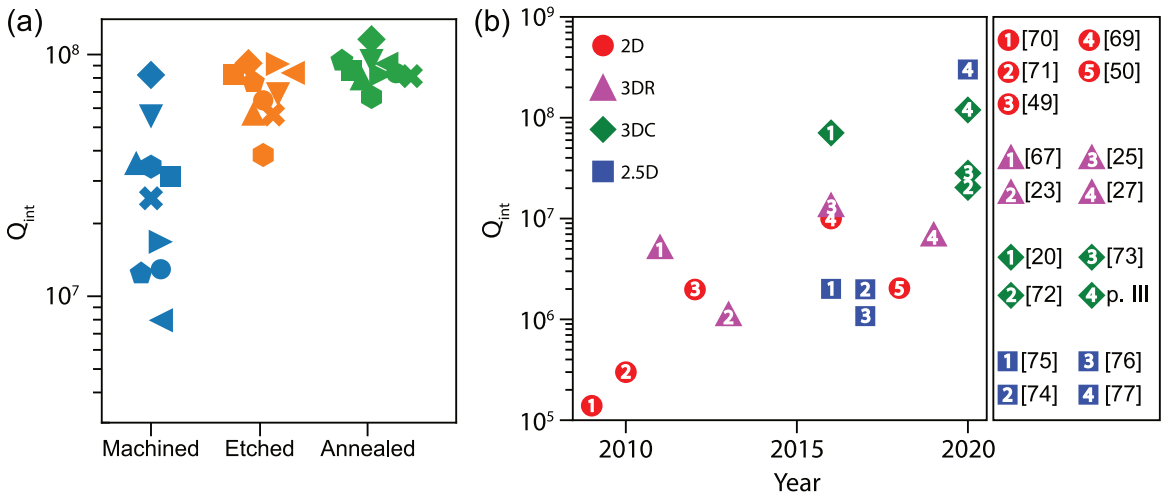

Figure 3.5: (a) Recipe for making reproducible 3D aluminum cavities with quality factors of 100 million. Each symbol represents one cavity made from 5N (99.999%) aluminum. Internal quality factor measured after machining (blue), etching (orange), and etching and annealing (green). (b) Adapted from [18]. Recipe from paper III(panel (a)) is compared with other work. Planar resonators are depicted in red circles [50, 49, 69, 70, 71], 3D rectangular cavities in purple triangles [25, 67, 23, 27], 3D stub geometry cavities [72, 20, 73] and paper III, and 2.5D cavities [74, 75, 76, 77].

3.7 Improving quality factor of 3D cavity resonators (Results summary)

From geometrical considerations, we understand that the participation ratios of all losses are orders of magnitude smaller in 3D cavities compared to coplanar circuits. This gives us a starting advantage when designing high-Q resonators. Now we should consider loss tangents themselves. When fabricating coplanar circuits we start from a pristine substrate with a low-loss tangent [67, 68]. The goal is then to deposit high-quality metal films and make sure all the surfaces are as defect-free as possible.

When we make a 3D cavity resonator we start from a high-purity block of material, but in the very first step, machining, we introduce strain and defects on the surface that was milled out. The goal now is to make this surface as defect-free as possible. In paper III we use etching, annealing, and electrochemical polishing in an attempt to increase the quality factor. We also try these surface treatments on aluminum of three different purities.

The recipe for reproducibly making aluminum cavities with quality factors of 90 million is presented in Fig. 3.5(a). Each cavity is represented by a symbol and each process by a color. The cavities differ in height and resonance frequency (details in paper III). Machining a block of 5N (99.999%) aluminum we get quality factors ranging from 8-82 million. After etching, the cavities have quality factors ringing from 44-98 million. Finally, after annealing the average quality factor is 88 million and the cavities have quality factors ranging from 66-115 million.

Our cavity was placed among other work in a review by Joshi et.al. [18] (Fig. 3.5(b)). We are proud that our recipe compares favorably with the work of others. As indicated in the review, we did not manage to keep this level of quality factor when we integrated the qubit. In fact, in papers IV, V, and VI we integrated a transmon qubit. The quality factors of the cavity modes in those papers are 7, 9, and 13 million respectively. We, unfortunately, did not measure those bare cavities (due to a lack of time), so we cannot tell if the qubit is indeed the limiting factor as we suspect. This is something that should be further investigated.

CHAPTER 4

Control and characterization of the resonator

In this chapter, we will define the resonator from a quantum mechanical perspective. We will see that driving the resonator with classical control pulses is not enough to reach universal control of the bosonic mode or to perform any computation faster than classical computers. This is what the ancilla qubit enables. We will go through the types of gates that dispersive coupling to a fixed frequency qubit paired with resonant driving enables. Finally, we will see how these gates allow us to both universally control the state of the resonator and to characterize the states and the gates we are implementing.

4.1 Limitations of the linear system

A resonator is a simple linear system described by the Hamiltonian:

$$H = \hbar\omega(a^\dagger a + 1/2) \tag{4.1}$$

here $\hbar$ is the reduced Planck constant, ω is the angular frequency of the mode, and $a^\dagger$ (a) is the creation (annihilation) operator. The energy spectrum is infinite and equidistant (see Fig. 4.1). If we drive the system with a classical field $\varepsilon(t)$, the driven Hamiltonian (with $\hbar = 1$ and

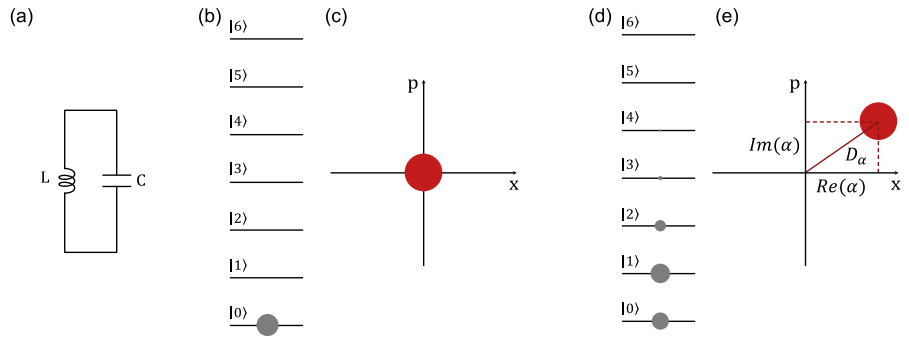

Figure 4.1: (a) Circuit representation of a resonator. (b) The energy spectrum of a linear resonator. Ground state in which only the vacuum state $|0\rangle$ is populated. (c) Representation of the vacuum state in phase space. (d) Coherent state Poissonian distribution of number states represented in the energy spectrum of a linear resonator. (e) Phase space representation of the coherent state α.

neglecting constant terms) becomes

$$H = \omega a^\dagger a + \varepsilon(t)\left(a\,\mathrm{e}^{i\omega t} + a^\dagger \mathrm{e}^{-i\omega t}\right) \tag{4.2}$$

where the frequency of the drive is the same as the frequency of the cavity. The evolution of such system is "trivial" in the sense that we can only ever create coherent states, and this is easily simulated on a classical computer. The evolution of the system is given by

$$U(t_0, t) = e^{\alpha a^\dagger - \alpha^* a} \equiv D_\alpha \tag{4.3}$$

where $\alpha = \int_{t_0}^{t} d\tau \varepsilon(\tau) e^{i\omega\tau}$ is the complex amplitude of the displacement. Starting from the vacuum state, the displacement operator D_α creates a coherent state

$$D_\alpha|0\rangle = |\alpha\rangle = e^{|\alpha|^2/2} \sum_n \frac{\alpha^n}{\sqrt{n!}}|n\rangle \tag{4.4}$$

The probability to find the resonator in Fock state $|n\rangle$ in a coherent state $|\alpha\rangle$ follows the Poisson distribution:

$$P_n(\alpha) = e^{-|\alpha|^2} \frac{|\alpha|^{2n}}{n!} \tag{4.5}$$

The expectation values of both position and momentum are defined as $\mathrm{Re}(\alpha)$ and $\mathrm{Im}(\alpha)$ and the uncertainty in both quadratures is the minimum prescribed by the Heisenberg uncertainty principle. The Wigner function (see Sec. 4.4 for more details) of the coherent state is a 2D Gaussian and is completely positive. Because of all these properties, coherent states are sometimes characterized as "almost quantum". However, displacements and coherent states are not enough, by themselves, to enable universal control of the bosonic mode or to enable quantum advantage. Nonetheless, they are a versatile resource that we can create with fidelities exceeding 99%. They will be one of the two gates that enable universal control of the bosonic mode [78] (see Sec. 4.5) and they will be our trusted probes when we characterize processes in the n-dimensional Hilbert space (see Sec. 4.6).

One solution to achieve universal control of a bosonic mode is to design a Hamiltonian that has terms that are at least cubic (i.e. $(a^\dagger)^M a^N$, with $M+N \geq 3$) [17]. Proposed implementation of this approach [79] requires frequency tunable circuits that are additionally subject to flux noise, which makes their coherence properties lower than their fixed frequency counterparts.

In this thesis we take the well-established approach of dispersively coupling a transmon qubit to a bosonic mode and we use this qubit for control and characterization of the bosonic mode.

4.2 Charge qubit in the transmon regime

There are a few reasons superconducting circuits make up such a good platform for quantum computing. First, the property of superconductors that makes them a good candidate is their very small resistive losses at microwave frequencies. The resistance is precisely zero only for DC currents. However, the resistive losses are very rarely the limiting factor for circuits made out of superconductors. For comparison, the internal quality factor at room temperature, limited by resistive loss, of cavities fabricated in paper III is around 2000. When cooled down to 10 mK the Q factor of the same cavities becomes limited by the dielectric losses at around $2 \cdot 10^8$, an improvement of five orders of magnitude. The second

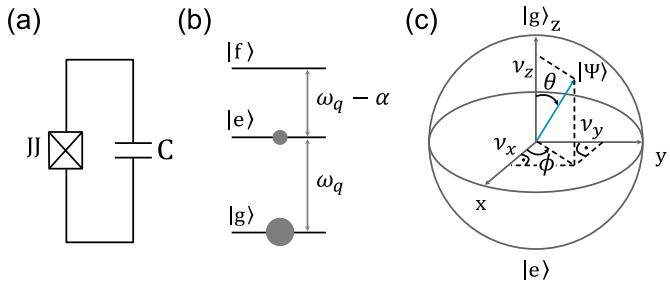

Figure 4.2: (a) Circuit model of the transmon qubit. A Josephson junction (JJ) is shunted by a capacitance C. (b) Energy spectrum of a transmon qubit. α here is the anharmonicity of the qubit. (c) Bloch sphere representation of a state of the qubit.

property is the size of the circuits, which is comparable to the wavelength of the microwaves. Hence, strong coupling between individual elements is easy to achieve. The most important property is the existence of the low-loss engineerable nonlinearity provided by Josephson junctions (JJs) [80]. The Josephson effect describes tunneling of Cooper-pairs between two superconductors separated by a thin tunnel barrier. It turns out that a JJ behaves like a nonlinear inductor

$$L_J = \frac{\hbar}{2eI_c} \frac{1}{\sqrt{1 - \left(\frac{I}{I_c}\right)^2}} \tag{4.6}$$

where L_J is the Josephson inductance that increases with increasing current I. This formula is valid for currents smaller than the critical current I_c.

The first qubit, demonstrated by Nakamura et al. [81], was a charge qubit in the Cooper-pair box regime characterized by $E_J/E_C \ll 1$, where $E_J = \hbar I_c/(2e)$ is the Josephson energy and $E_C = e^2/(2C)$ is the charging energy. In this regime, the charge qubit is susceptible to charge noise. The transmon qubit [82] (Fig. 4.2) is a charge insensitive variant of the charge qubit. This regime is characterized by $E_J/E_C \gg 1$. The charging energy sets the anharmonicity of the transmon qubit, and the Hamiltonian is described approximately as:

$$H = \hbar\omega_q b^\dagger b - \frac{E_c}{2} b^\dagger b^\dagger b b \tag{4.7}$$

The transmon frequency is set by $\hbar\omega_q = \sqrt{8E_C E_J} - E_C$.

In our experiments, we use a transmon qubit as the ancilla with a self-Kerr $\alpha = E_C/\hbar \approx 2\pi \times (200 - 300)$ MHz. In most of our experiments, we use only the first two levels of the transmon qubit $|g\rangle$ and $|e\rangle$ (Fig. 4.2), and we always make sure our drives are such that they do not excite the higher states. In this case, we can simplify the qubit Hamiltonian ($\hbar = 1$):

$$H = \frac{\omega_q}{2}\sigma_z \tag{4.8}$$

where σ_z is the Pauli z operator and any pure state of the qubit can be represented on the surface of a Bloch sphere (Fig. 4.2)

$$|\Psi\rangle = \cos(\theta/2)|g\rangle + e^{i\phi}\sin(\theta/2)|e\rangle \tag{4.9}$$

And in general, any state of the qubit can be represented by a density matrix

$$\rho = \frac{1}{2}\left(I + \nu_x\sigma_x + \nu_y\sigma_y + \nu_z\sigma_z\right) \tag{4.10}$$

where (ν_x, ν_y, ν_z) are projections of the vector representing the qubit state onto axis (x, y, z) (Fig. 4.2), and σ_x, σ_y and σ_z are the Pauli operators.

Universal control of a single qubit is simple. Any qubit rotation around axis ϕ for angle θ ($R_\phi(\theta)$) is easily implemented with classical drives oscillating at the frequency of the qubit, and having appropriate phases and envelope shapes.

4.3 Dispersive coupling to a transmon qubit

Now that we understand both the resonator and the qubit representations as circuits and their Hamiltonians, coupling them to each other is easy. We bring them close together, so that the electric field of the resonator overlaps with the dipole moment of the plates forming the capacitance of the qubit. In circuit terms, this forms a coupling capacitance C_{qc} (Fig. 4.3). The Hamiltonian is described by the individual

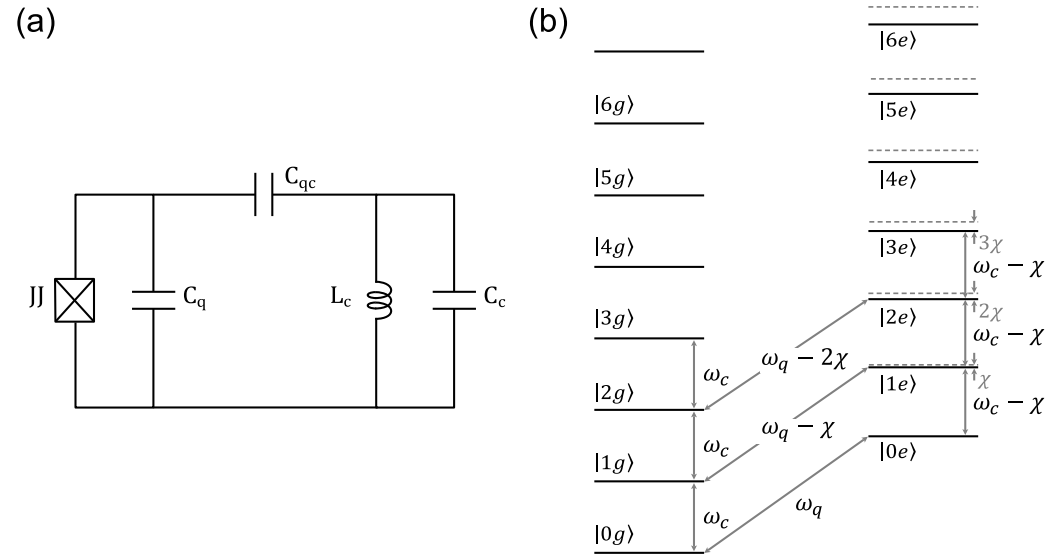

Figure 4.3: (a) Circuit representation and (b) energy spectrum of a resonator dispersively coupled to the two levels of a qubit. The dispersive coupling χ modifies the frequency of both the resonator and the qubit depending on the state of the other.

Hamiltonians of each element plus the interaction term, which forms the Jaynes-Cummings Hamiltonian [83]:

$$H = \omega_c a^\dagger a + \frac{\omega_q}{2}\sigma_z + g(a^\dagger \sigma_- + a\sigma_+) \tag{4.11}$$

In the case of large detuning ($\Delta = |\omega_c - \omega_q| \gg g$) we can approximate the Jaynes-Cummings Hamiltonian with a dispersive model:

$$H = \omega_c a^\dagger a + \frac{\omega_q}{2}\sigma_z + \frac{\chi}{2} a^\dagger a \sigma_z \tag{4.12}$$

where $\chi = g^2/\Delta$ is the dispersive shift. This is an exact solution for the dispersive shift for a two-level system. Taking into account qubit self-Kerr, the dispersive shift gets modified:

$$\chi = \frac{g^2}{\Delta}\frac{\alpha}{\alpha - \Delta}. \tag{4.13}$$

The dispersive interaction manifests itself as a frequency shift of each mode depending on the occupation number of the other mode. The frequency of the resonator is shifted by χ depending on the state of

the qubit, and equivalently, the frequency of the qubit will be shifted by $n\chi$ depending on the number of photons in the cavity (Fig. 4.3). If all the dissipation rates of the qubit and the cavity are smaller than the dispersive shift, $\kappa_q, \kappa_c \ll \chi$, we are able to perform gates that are selective on the state of either the qubit or the cavity simply by applying drives at the appropriate frequencies. If we stick to resonant drives, there are a few "obvious" operations we can perform:

1. Unselective cavity displacements D_α
2. Unselective qubit rotations about an axis $R_\phi(\theta)$
3. Entangling conditional phase $C_\phi = e^{i\phi a^\dagger a|e\rangle\langle e|}$
4. Selective cavity displacements $D_\alpha|g\rangle\langle g| + I_a|e\rangle\langle e|$
5. Selective qubit rotations $|n\rangle\langle n|R_\phi(\theta) + (I_a - |n\rangle\langle n|)I_q$

I_a (I_q) is the identity operator on the cavity (qubit) Hilbert space. The unselective cavity displacement is precisely what we described in Sec. 4.1. We implement it by applying a short resonant pulse at the cavity frequency. This will produce an unselective drive if the width of the pulse in the frequency domain is much larger than χ. Similarly, unselective qubit rotations are implemented with short pulses resonant with the qubit frequency. Hence, the width of the pulses in the frequency domain has to be larger than $n\chi$ if we want the pulse to be unselective for up to n Fock states.

We get the entangling conditional phase operation "for free" by letting the Hamiltonian evolve in time. The angle $\phi = t\chi$ depends on the evolution time and the dispersive shift χ. As we will see in Sec. 4.4, this operation can be used to map the parity of the cavity field onto the qubit.

The selective cavity displacement is implemented by a long pulse resonant with ω_c or $\omega_c - \chi$ to make it selective on the ground or the excited state of the qubit, respectively. Here the length of the pulse should be much longer than $1/\chi$. For the selective qubit rotations, we send a

long pulse resonant with $\omega_q - n\chi$ in order to drive a rotation selective on Fock number n. The selective number-dependent arbitrary phase (SNAP) gate is a special case of the selective qubit rotations. SNAP gates and unconditional displacements are enough for universal control of a bosonic mode (see more in Sec. 4.5).

4.3.1 Corrections to the ideal dispersive Hamiltonian

Unfortunately, when we couple a strongly nonlinear mode, such as the transmon qubit, to the linear mode of the cavity, the modes hybridize and the cavity mode inherits a little bit of nonlinearity from the transmon. The relevant Hamiltonian is then:

$$H = \omega_c a^\dagger a + \frac{K_c}{2} a^\dagger a^\dagger a a + \omega_q q^\dagger q + \frac{\alpha_q}{2} q^\dagger q^\dagger q q + \chi a^\dagger a q^\dagger q + \frac{\chi'}{2} a^\dagger a^\dagger a a q^\dagger q \tag{4.14}$$

In our system, the cavity self Kerr K_c is usually a few kHz, and the correction to the dispersive shift χ' is about 10-20 kHz. These are small corrections compared to qubit self-Kerr $\alpha_q \approx$ 200-300 MHz and the dispersive shift $\chi \approx$ 1-3 MHz. However, they are comparable to qubit and cavity dissipation rates (around 2-8 kHz for the qubit and around 500-800 Hz for the cavity). It is therefore necessary to take these corrections into account to maximize the fidelities of the bosonic states and gates we want to prepare in the cavity.

In our system in papers IV-VI, we have an additional readout resonator that is patterned on the same chip as the qubit. The readout resonator is dispersively coupled to the qubit and is exclusively used to probe its state. We will omit this mode in the following discussions about the control of the cavity mode, and whenever we refer to the resonator, what we really mean is the cavity. This is not to say that the readout resonator mode does not have any use beyond the readout of the qubit state. On the contrary, having a mode strongly coupled to the transmission line can be really useful. For example, the readout resonator was used to reset the state of the cavity [84], reset the qubit [85], and it is crucial for autonomous quantum error-correction [24] and error-suppression [86] as a place to dump excitation.

The first experiment that we perform in papers IV-VI is system calibration. The system calibration is measuring all the parameters in Eq. 4.14 plus decoherence and dephasing times of both the cavity and the qubit. All of the parameters are listed in the supplementary information of the papers and the calibration procedure is detailed in Appendix A. This is a standard procedure and has been described before for example in [87]. We will list it out explicitly in Appendix A.

4.4 Probing the state of the cavity

We can probe the state of the cavity in two different ways. We can map the population of individual Fock states onto the population of the qubit, or we can map the cavity state's parity onto the qubit's population. Measuring only populations of the Fock states is not enough to completely characterize the bosonic state, but it's a useful tool. It is implemented by applying a selective π pulse whose frequency we select to be $\omega_q - n\chi$, where n depends on which Fock states we are interested in. The population of the qubit at each frequency $\omega_q - n\chi$ is directly proportional to the population of each Fock state $|n\rangle$.

The Wigner function $W(\alpha)$ is a quasi-probability distribution, which uniquely describes a bosonic state. It is defined as the scaled expectation value of the parity operator:

$$P = e^{i\pi a^\dagger a} \tag{4.15}$$

in each point of the phase space:

$$W(\alpha) = \frac{2}{\pi} Tr(D_\alpha^\dagger \rho D_\alpha P) \tag{4.16}$$

Notice that α is a complex displacement amplitude. $W(\alpha)$ can take both positive and negative values. Negative values, so-called Wigner negativity, is what makes a state nonclassical and is a necessary resource for quantum advantage [88, 89].

To measure the Wigner function in the point $W(\alpha)$, we typically initiate the qubit in the ground state (although the qubit can be initiated in the excited state). Next, we should apply displacements $D_{-\alpha}$ to map

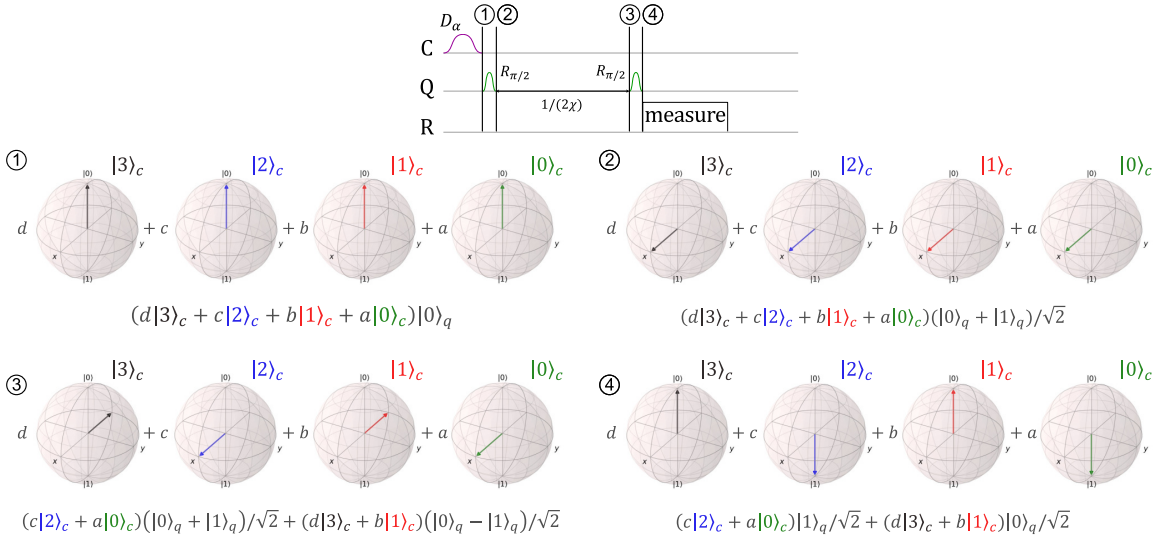

Figure 4.4: Pulse sequence to measure Wigner function with step-by-step state transformation showing the mapping of the parity of the cavity onto the population of the qubit.

different parts of the phase space. Now we map the parity of the cavity state to the population of the qubit. We do this by applying two unselective $\pi/2$ pulses separated by a waiting time of $1/(2\chi)$. In our experiments χ takes values from 1.5-3 MHz, so the waiting time is around 166-333 ns. We are applying a special case of entangling conditional phase gate, where all the even Fock states are going to end up mapping to the excited state of the qubit, and all the odd states will map to the ground state of the qubit (see Fig. 4.4).

Once we have measured the Wigner function, finding the density matrix that best fits the measured data is not trivial. It is common to use a method called maximum likelihood estimation [90]. However, we opted for using the gradient descent approach [91, 92], because of its ability to perform reconstruction for large dimensions of Hilbert space and with noise present in the data.

4.5 Creating arbitrary states and gates

It has been proven that by applying an interleaved sequence of displacement and SNAP gates, one can implement any unitary on the bosonic mode [78]. Not only is this control universal, but it is efficient [93] in

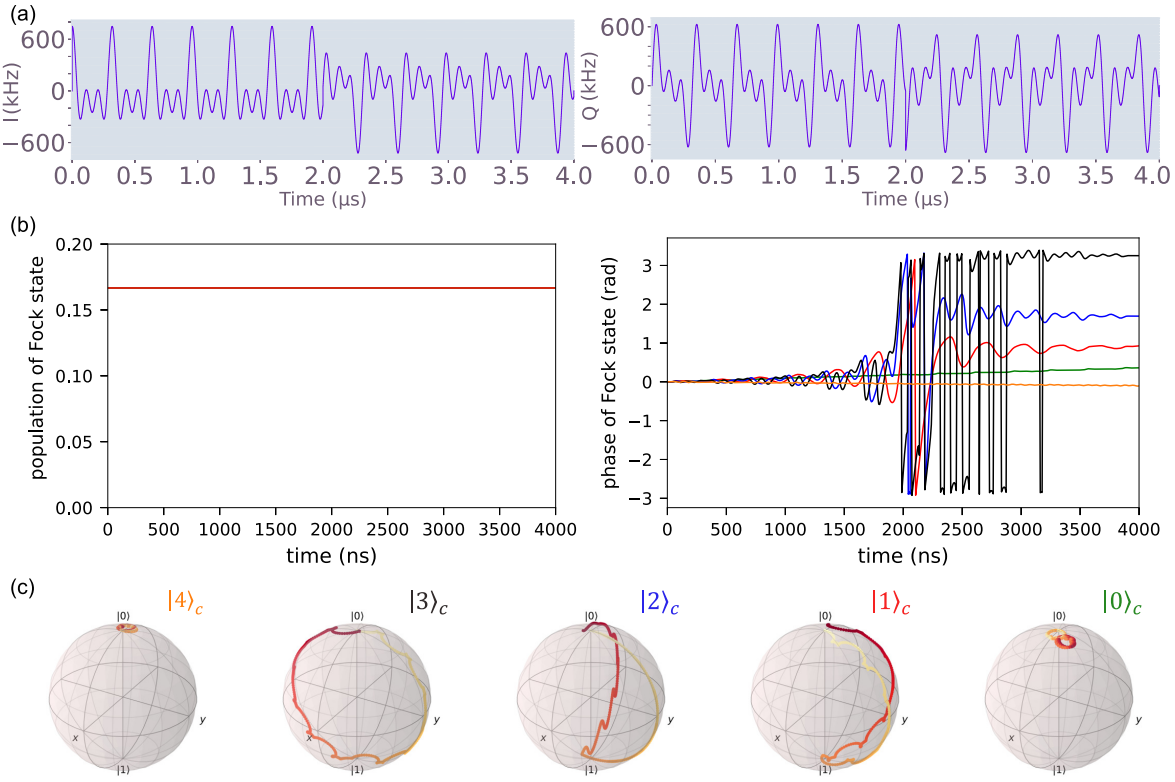

Figure 4.5: Example of standard SNAP gate $S(0, \pi/4, \pi/2, \pi, 0)$. (a) Pulse envelopes are a sum of *pi* pulses at frequencies $n\chi$, (b) evolution of Fock state populations and phases during the SNAP gate. Each Fock state $|n\rangle$ is represented by a color. We initiate the cavity state in an equal superposition of all the Fock states from $|0\rangle$ to $|5\rangle$. (c) Bloch representation of the evolution of qubit state conditioned on the cavity state $|n\rangle$.

the sense that very few gates are needed in order to achieve high-fidelity bosonic states and gates.

4.5.1 Standard SNAP gates

As we mentioned earlier, SNAP gates [94] are a special case of selective qubit rotations. SNAP gate that adds an arbitrary phase θ_n to Fock state $|n\rangle$ is defined as

$$S_n(\theta_n) = e^{i\theta_n |n\rangle\langle n|}. \tag{4.17}$$

In general, a SNAP gate can add any phase to any Fock state $|n\rangle$ simultaneously

$$S(\vec{\theta}) = \prod_{n=0}^{m} e^{i\theta_n |n\rangle\langle n|}. \tag{4.18}$$

To implement a SNAP gate $S_n(\theta_n)$, we apply two consecutive selective π pulses whose axis of rotation are separated by θ_n. The frequency of the selective π pulses is $\omega_q - n\chi$, for each Fock level n, respectively, and each individual π rotation has to be long such that the duration $T \gg 1/\chi$. Implementing a SNAP gate that adds multiple phases to multiple Fock states $S(\vec{\theta})$ comes down to applying a sum of individual SNAP components $S_n(\theta_n)$. Since frequencies are well separated by χ, it is very easy to calibrate SNAP gates individually. All we need to do is to measure the qubit frequency ω_q, the dispersive shift χ, the Rabi rate ω_{Rabi}, the correction to the dispersive shift χ' and the cavity Kerr K_c (see Appendix A).

An example of implementing a standard SNAP gate $S(0, \pi/4, \pi/2, \pi, 0)$ is given in Fig. 4.5(a). We used the dispersive shift $\chi/(2\pi) = 3.14$ MHz (same as in paper IV). The gate time is $4\,\mu$s $\approx 12(2\pi)/\chi$. We initiate the cavity state in an equal superposition of states $\frac{1}{\sqrt{6}}\sum_{n=0}^{5}|n\rangle$. A SNAP gate does not change the population of the cavity state (see Fig. 4.5(b)). Since the SNAP gate is a sum of π pulses with frequencies $\omega_q - n\chi$, it is obvious that this drive will not influence the cavity populations. The phase evolution during the SNAP gate (Fig. 4.5(b)) is ideally a Heaviside step function with the step happening at half the gate time. After the entire duration of the gate, the phase error is up to ± 0.3 rad. This is because the gate time is still too short and multiple frequency components are driving the neighboring transitions. We did not include any decoherence in our simulation, so all the errors are coherent errors. Another way to visualize evolution during the gate is to represent the qubit evolution on Bloch spheres conditioned on cavity being in Fock state $|n\rangle$ (Fig. 4.5(c)). The evolution is close to the one we expect from two π pulses. However, we can clearly see that states conditioned on the cavity being in state $|0\rangle$ and $|4\rangle$ that are not supposed to move from the ground state are in fact moving slightly.

Since the evolution of the cavity mode under the Kerr term is just deterministically adding phases to Fock states, SNAP gates are ideal to cancel this evolution.

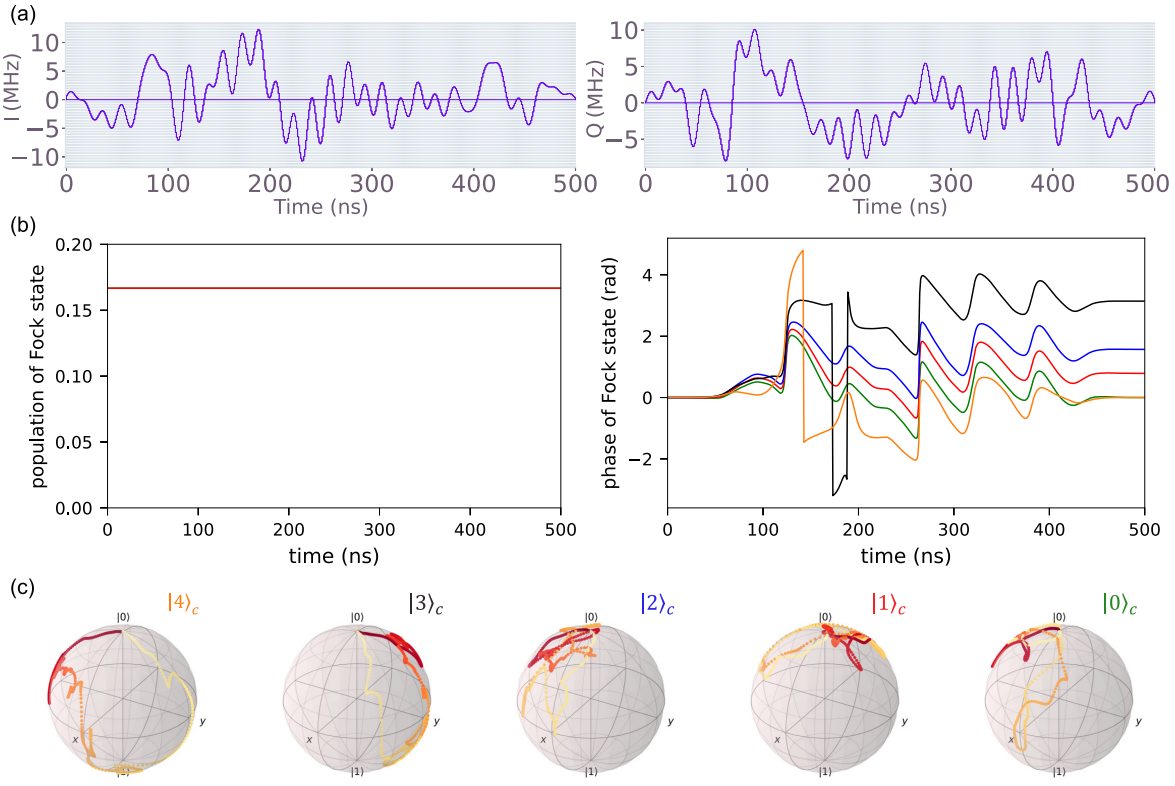

Figure 4.6: Example of optimized SNAP gate $S(0, \pi/4, \pi/2, \pi, 0)$. (a) Pulse envelopes, (b) evolution of Fock state populations and phases during the SNAP gate. Each Fock state $|n\rangle$ is represented by a color. We initiate the cavity state in an equal superposition of all the Fock states from $|0\rangle$ to $|5\rangle$. (c) Bloch representation of the evolution of qubit state conditioned on the cavity state $|n\rangle$.

4.5.2 Optimized SNAP gates

In order to make SNAP gates as short as possible $T \approx 1/\chi$ we can optimize the envelopes of the microwave drives that we apply. We use an optimizer [95] that needs the parameters of Hamiltonian from Eq. 4.14. The Hamiltonian in Eq. 4.14 is supplemented by a qubit drive term with discretized envelope whose amplitudes are optimized to implement the desired SNAP gate. In order for the pulses that the optimizer finds to be implemented in the laboratory, we need to limit the maximum Rabi rate, the bandwidth, and the sampling frequency of the pulses. The upside of optimizing the SNAP envelopes is that we do not need to do any extra calibration experiments compared to calibrating the standard SNAP gates.

An example of an optimized SNAP gate $S(0, \pi/4, \pi/2, \pi, 0)$ is given

in Fig. 4.6(a). We used the dispersive shift $\chi/(2\pi) = 3.14$ MHz, maximum Rabi rate 20 MHz, the cutoff frequency for the maximum bandwidth 60 MHz and the sampling frequency 1 Gs/s (same as in paper IV and standard SNAP example in Fig. 4.5). The gate time is 500 ns $\approx 1.5(2\pi)/\chi$ which is 8 times shorter than the standard SNAP gate described in Sec. 4.5.1. We again initiate the cavity state in an equal superposition of states $\frac{1}{\sqrt{6}}\sum_{n=0}^{5}|n\rangle$. The SNAP gate does not change the population of the cavity state (Fig. 4.6(b)). Since the SNAP gate center frequency is the qubit frequency ω_q and the bandwidth of the optimized SNAP pulses is always chosen to be a few tens of MHz, it is obvious that this drive will not influence the cavity populations. The phase evolution during the SNAP gate (Fig. 4.6(b)) is not something we could predict without running the simulation. After the entire duration of the gate, the phases added are what we wanted, namely $0, \pi/4, \pi/2, \pi, 0$ for Fock states $|0\rangle$ to $|5\rangle$ respectively. Another way to visualize the evolution during the gate is to represent the qubit evolution on Bloch spheres conditioned on cavity being in Fock state $|n\rangle$ (Fig. 4.6(c)). The evolution is clearly more complicated than in the case of standard SNAP gates (see Fig. 4.5(c)).

4.5.3 Wigner negative states with displacement and SNAP gates (Results summary)

In order to maximize the fidelity of bosonic states and gates created by interleaved sequences of displacement and SNAP gates, we need to ensure two things: i) we should apply the smallest number of gates to achieve the target fidelity and ii) make individual gates as short as possible. This is exactly what we do in paper IV in order to create arbitrary bosonic states in the 3D cavity. In paper V we use this technique to apply a bosonic X-gate on a binomially encoded bosonic qubit.

We use a two-step optimization (Fig. 4.7(b)). First, we optimize the parameters of displacement and SNAP gates [93] in order to get the best possible fidelity of the target state. Second, we reduce the length of the SNAP gates by optimizing their pulse envelopes.

The states that we can prepare with two SNAP gates are Fock state $|2\rangle$, binomial state $(|0\rangle + |4\rangle)/\sqrt{2}$ and an odd cat state $(|\alpha\rangle - |-\alpha\rangle)/\lambda$,

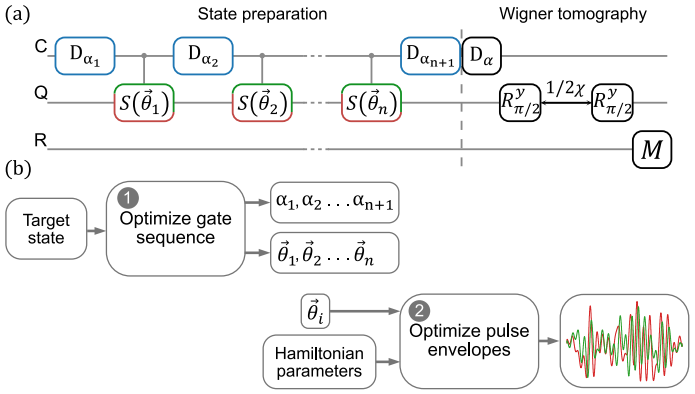

Figure 4.7: (a) Pulse sequence used to prepare and characterize the Wigner negative states. D_{α_i} are the displacement and $S(\vec{\theta}_i)$ are the SNAP gates. Wigner tomography is explained in Sec. 4.4. (b) The two steps of optimization that we perform to find the desired displacement and SNAP gates.

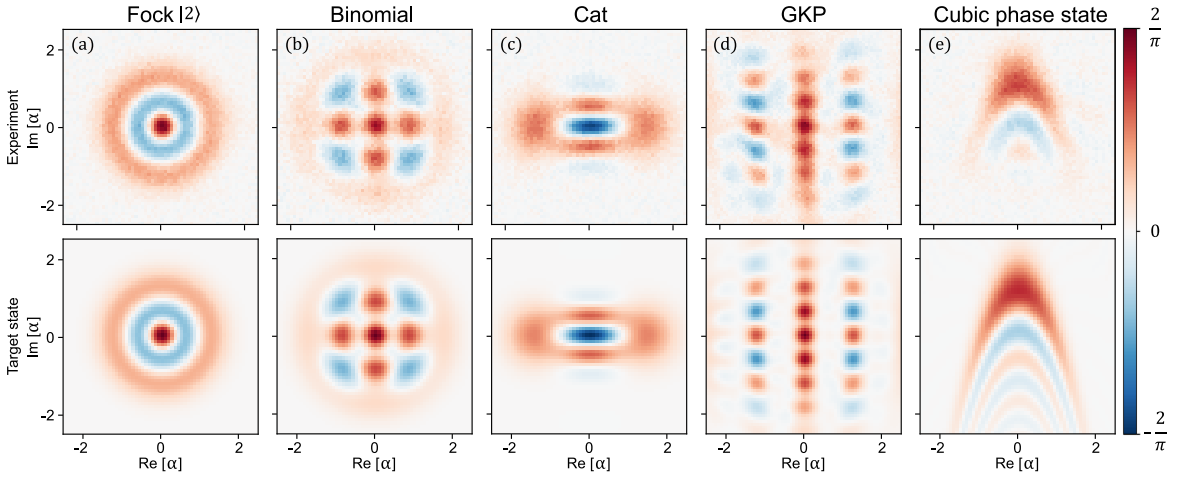

Figure 4.8: Examples of states we can create with displacement and SNAP gates. (a) Two-photon Fock state $|2\rangle$, (b) binomial state $(|0\rangle + |4\rangle)/\sqrt{2}$, and (c) an odd cat state $(|\alpha\rangle - |-\alpha\rangle)/\lambda$, with $\alpha = \sqrt{2}$ and λ the normalization constant. These three states have 2 photons on average and were created with two SNAPs and three displacements. Next, (d) the GKP state with four photons on average and (e) the cubic phase state. The GKP state was prepared with three SNAPs and four displacements and the cubic phase state was prepared with three SNAPs and three displacements.

with $\alpha = \sqrt{2}$ and λ the normalization constant (see Fig. 4.8(a)-(c)). We prepared these states with fidelities 0.99, 0.94, and 0.96 respectively. More surprisingly, we were able to prepare a Gottesman-Kitaev-Preskill (GKP) state and a cubic phase state (see Fig. 4.8(d)-(e)) using three SNAP gates. We prepared these states with the fidelity of 0.93 and 0.92, respectively. The reason we found this surprising is that both GKP

and cubic phase state have a rather complicated structure. The Wigner functions of these states have a lot of alternating positive and negative regions. GKP states were only recently demonstrated using conditional displacement gates in both superconducting circuits and trapped-ions [30, 31]. To date, to the best of our knowledge, this is the only experimental demonstration of a cubic phase state.

We found one more curious fact about optimized SNAP gates. They are 5 times less sensitive to the calibration of dispersive shift χ, and 7 times less sensitive to fluctuations of qubit frequency compared to standard SNAP gates. We suspect that it has to do with the fact that optimized SNAP gates have continuous support in frequency space up to a cutoff while standard SNAP gates have peaks centered at frequencies $\omega_q - n\chi$ making them sensitive to changes in these two parameters.

4.6 Process tomography of a large Hilbert space (Results summary)

We already showed that by measuring the Wigner function we can determine the state of the cavity mode. From the Wigner data we can reconstruct the $n \times n$ density matrix. In order to characterize a bosonic gate or process we need to describe a quantum process matrix that maps the initial $n \times n$ density matrix into the final $n \times n$ density matrix. This quantum process matrix has dimensions $n^2 \times n^2$.

Often we will encode the state of the logical qubit into a suitable encoding, e.g. binomial encoding. This encoding spans a binary logical subspace within the n-dimensional Hilbert space of the resonator. Sometimes we are only interested in the gate fidelity within this logical subspace. Then it is possible to use encoding and decoding operations [96] that map the state of the ancilla qubit into the logical subspace and vice versa. We could sandwich the bosonic gate we are interested in with the encoding and decoding gates and use all the standard qubit gate measurements such as e.g. qubit process tomography [97] or randomized benchmarking [98] to assign the fidelity to the bosonic gate. This approach has two limitations. The first limitation is that the encoding and decoding operations often have similar fidelity as the bosonic gates

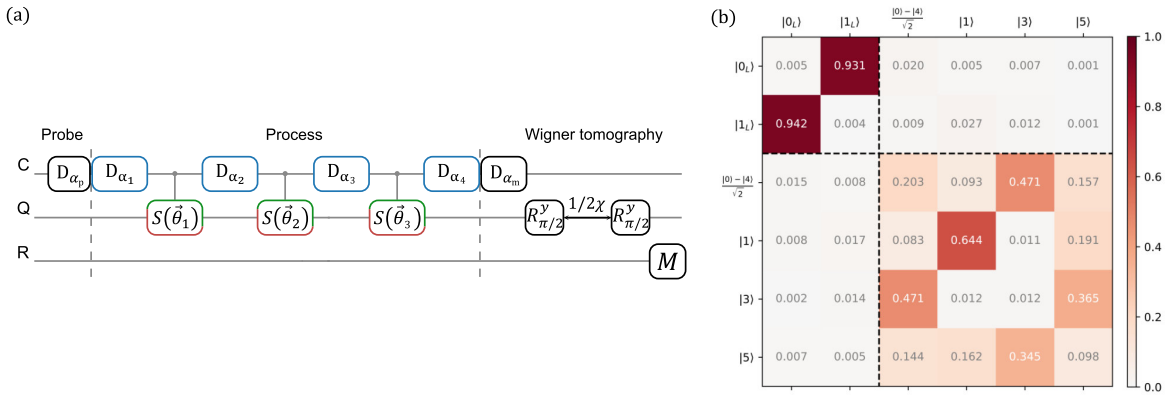

Figure 4.9: (a) Process tomography is divided into three parts. Preparation of the probe coherent states α_p, applying the process (in our example X-gate on binomial encoding) and measuring Wigner function in points α_m. (b) Measured population transfer matrix for X-gate on binomial encoding implemented by four displacements and three SNAP gates.

that we are trying to characterize, therefore they cannot be considered as "trusted" operations. The second limitation is that the $n^2 \times n^2$ dimensional process matrix is getting reduced to a 4×4 process matrix of the binary system. This means that we are not able to distinguish incoherent errors from, for example, leakage errors, which we might be able to avoid by calibrating our gate better.

The technique that improves on these two limitations is the coherent state process tomography. It was previously used in quantum optics together with homodyne detection in order to characterize bosonic gates [99, 100]. We adopt this technique and advance it by replacing the homodyne measurements with Wigner function measurements. Furthermore, a major difference is that we combine it with the gradient-descend based learning algorithm [101] that reconstructs the quantum process matrix from very limited data. This way we get the full $n^2 \times n^2$ process matrix and avoid using the complex encoding and decoding gates.

The coherent-state process tomography consists of three parts. Preparation of a probe state, which we choose to be a coherent state. We can prepare these states with fidelities exceeding 99%, meaning that they are "trusted" states. We apply the process or a gate that we want to characterize, and finally, we measure the Wigner function of the resulting state (see Fig. 4.9(a)). Then the procedure is repeated for a matrix of

probe states spanning the part of the Wigner space of interest. Because of the reconstruction algorithm we are using, we are able to reconstruct the process matrix of the binomial X-gate using only 5×5 probe states and 21×21 Wigner points.

There are different representations of the process matrix. One of the easiest to understand is the population transfer matrix presented in Fig. 4.9(b). It does not contain the full information contained in the process matrix, but it allows us to spot certain kind of errors easily. The top left corner of the matrix represents the logical subspace. Ideally, matrix elements $|0_L\rangle\langle 1_L|$ and $|1_L\rangle\langle 0_L|$ should be 1, and all the other elements in the first two columns and first two rows should be 0. Importantly, the non-zero elements outside the top left square of the transfer matrix indicate leakage outside the computational subspace, information that is typically inaccessible when using the encode-decode process tomography protocol.

From this and other representations (see paper V for more details), we can learn how the bosonic gate is acting on a large Hilbert space of the resonator, which is another useful tool in our bosonic toolkit.

CHAPTER 5

Off-resonant drives

As we discussed in the previous chapter, driving the dispersively coupled cavity-qubit system on resonance with either mode enables universal control of the cavity mode. We chose to use unselective displacements and a special case of selective qubit rotations (SNAP gates) in papers IV and V to control the cavity mode. It has been shown that a complementing pair of operations, namely the special case of selective displacements (echoed conditional displacements) and unconditional qubit rotations will do the same [66]. The upside of resonant driving is that the drives do not induce Stark shifts of the modes, meaning they can be calibrated independently of each other. However, just because a set of gates forms a universal set, it does not mean they are the best way to implement a particular gate. For example, selective displacements are well-suited for correcting small displacement errors as demonstrated in the successful implementation of quantum error correction on GKP encoding [32, 30]. However, SNAP gates are much better suited to adding the phases to individual Fock states. It would be inefficient to use displacement and SNAP gates to implement conditional displacements and vice versa - it would be inefficient to use conditional displacements and unselective qubit rotations to implement a SNAP gate.

This is why we decided to explore off-resonant driving to implement selective single photon addition. In our implementation, off-resonant drives simultaneously selectively add a photon and excite the qubit depending on the cavity state. Even though it could be implemented with displacement and SNAP gates, we found a more efficient way to do it. Off-resonant drives will introduce Stark shifts and we have to consider more Hamiltonian terms to try and capture the results we measure in paper VI.

5.1 Hamiltonian derivation

Our derivation closely follows the derivation in [102]. Our starting point is the Hamiltonian of a coupled qubit-cavity system described by:

$$H = \omega_a a^\dagger a + \omega_q q^\dagger q + \frac{E_J}{4!}\left[\varphi_q(q+q^\dagger)\right]^4 - g\left(q-q^\dagger\right)\left(a-a^\dagger\right), \tag{5.1}$$

where we neglect all terms higher than the fourth order in the expansion of the Josephson cosine potential and g is the coupling strength between the qubit and the cavity. One can diagonalize (5.1) and get

$$H = \omega_a a^\dagger a + \omega_q q^\dagger q - \frac{E_J}{4!}\phi^4, \tag{5.2}$$

where ω_a and ω_q already include contributions due to the quadratic part of the Josephson potential and

$$\phi = \varphi_q(q+q^\dagger) + \varphi_a(a+a^\dagger), \tag{5.3}$$

is the total flux field across the junction with φ_q and φ_a the participation ratios of the qubit and cavity modes, respectively. The goal is to drive transitions from $|n\rangle|g\rangle$ to $|n+1\rangle|e\rangle$, selectively, i.e., we perform a two excitation transition where we excite the qubit and add a photon to the cavity only if the cavity is in Fock state $|n\rangle$. In order to achieve this, we are going to drive both the cavity and the qubit off-resonance. The total Hamiltonian of the driven system is

$$\begin{aligned} H(t) &= \omega_q q^\dagger q + \omega_a a^\dagger a - \frac{E_J}{4!}\phi^4 \\ &+ \epsilon_1\left(q\,\mathrm{e}^{i\omega_1 t} + q^\dagger \mathrm{e}^{-i\omega_1 t}\right) + \epsilon_2\left(a\,\mathrm{e}^{i\omega_2 t} + a^\dagger \mathrm{e}^{-i\omega_2 t}\right), \end{aligned} \tag{5.4}$$

where ϵ_1 and ϵ_2 are the strengths of the qubit and cavity drives, respectively, with frequencies ω_1 and ω_2. We eliminate the linear terms in (5.4) by means of the time-dependent displacement transformation

$$D(t) = \exp\left(\xi_1 \mathrm{e}^{-i\omega_1 t} q^\dagger - \bar{\xi}_1 \mathrm{e}^{+i\omega_1 t} q\right) \exp\left(\xi_2 \mathrm{e}^{-i\omega_2 t} a^\dagger - \bar{\xi}_2 \mathrm{e}^{+i\omega_2 t} a\right). \quad (5.5)$$

The Hamiltonian in the displaced frame is then

$$\begin{aligned} H(t) &= \omega_q q^\dagger q + \omega_a a^\dagger a \\ &- \frac{E_J}{4!}\left[\varphi_q\left(q - \xi_1 \mathrm{e}^{-i\omega_1 t}\right) + \varphi_a\left(a - \xi_2 \mathrm{e}^{-i\omega_2 t}\right) + \text{h.c.}\right]^4. \end{aligned} \quad (5.6)$$

Here, the amplitudes ξ_i, $i = 1, 2$ are given by

$$\xi_1 = \frac{\epsilon_1}{\Delta_1}, \quad (5.7)$$

$$\xi_2 = \frac{\epsilon_2}{\Delta_2}, \quad (5.8)$$

where Δ_1 and Δ_2 are the detunings of the qubit and cavity drives respectively. Regardless of the drive frequencies, the fourth-order interaction yields the following nonrotating (nr) contributions

$$H_{\text{nr},1} = -\frac{\alpha_q}{2} q^{\dagger 2} q^2 - \frac{K_c}{2} a^{\dagger 2} a^2 - \chi\, q^\dagger q\, a^\dagger a, \quad (5.9)$$

$$H_{\text{nr},2} = \delta_{\text{Stark},q}\, q^\dagger q + \delta_{\text{Stark},a}\, a^\dagger a. \quad (5.10)$$

The Hamiltonian (5.9) corresponds to the drive-independent terms. Here α_q is the qubit anharmonicity, K_c is the Kerr nonlinearity of the cavity, and χ is dispersive interaction (cross-Kerr) between the qubit and the cavity. Furthermore, the corresponding interaction strengths are given by

$$\alpha_q = \frac{E_J\, \varphi_q^4}{2}, \quad (5.11)$$

$$K_c = \frac{E_J\, \varphi_a^4}{2}, \quad (5.12)$$

$$\chi = E_J\, \varphi_a^2\, \varphi_q^2. \quad (5.13)$$

On the other hand, the Hamiltonian (5.10) corresponds to the drive-activated quadratic terms, i.e., the ac Stark shifts or frequency shifts

due to the drives. These are given by

$$\delta_{\text{Stark},q} = -2\,\alpha_q\,|\xi_1|^2 - \chi\,|\xi_2|^2, \tag{5.14}$$
$$\delta_{\text{Stark},a} = -2\,K_c\,|\xi_2|^2 - \chi\,|\xi_1|^2. \tag{5.15}$$

The time-dependent term corresponding to this effective drive is

$$H_{\text{drive}}(t) = \xi_{\text{eff}}\,\mathrm{e}^{-i(\omega_1+\omega_2)t}\,q^\dagger a^\dagger + \text{h.c.}, \tag{5.16}$$

where the effective drive strength is given by

$$\xi_{\text{eff}} = -E_J\varphi_q^2\varphi_a^2\xi_1\xi_2 = -\chi\xi_1\xi_2. \tag{5.17}$$

Together with (5.6) we obtain $H(t) = H_{\text{nr},1} + H_{\text{nr},2} + H_{\text{drive}}(t)$ as the following

$$\begin{aligned} H(t) &= (\omega_q + \delta_{\text{Stark},q})\,q^\dagger q + (\omega_a + \delta_{\text{Stark},a})\,a^\dagger a - \frac{\alpha_q}{2}q^{\dagger 2}q^2 \\ &- \frac{K_c}{2}a^{\dagger 2}a^2 - \chi q^\dagger q\,a^\dagger a + \left(\xi_{\text{eff}}\,q^\dagger a^\dagger \mathrm{e}^{-i(\omega_1+\omega_2)t} + \text{h.c.}\right). \end{aligned} \tag{5.18}$$

The purpose of the drives is to allow for the number-selective simultaneous excitation of the cavity and the qubit. As stated above, the goal is to induce transitions of the form $|n\rangle|g\rangle \to |n+1\rangle|e\rangle$. Instead of driving them directly, we are going to consider driving them via a virtual state detuned by some detuning Δ. Thus, in order to activate this two-excitation process we require that the frequencies of both drives add to the corresponding transition frequency. In the presence of the Stark shifts, the energy of exciting the qubit is $\omega_q + \delta_{\text{Stark},q} - n\chi$ depending on the state of the cavity, while the energy of adding a photon to the cavity is $\omega_a + \delta_{\text{Stark},a}$. Thus, the total frequency of this two-excitation transition is given by

$$\omega_1 + \omega_2 = (\omega_q + \delta_{\text{Stark},q}) + (\omega_a + \delta_{\text{Stark},a} - \chi)\,. \tag{5.19}$$

We note that we should have additional higher-order terms resulting from the four-wave mixing of the cavity, qubit, and driving fields in (5.18). However, for now, we neglect them as they are not resonant terms. Number selectivity imposed $\xi_{\text{eff}} < \chi$, therefore from (5.17), we require $\epsilon_i < \Delta_i$.

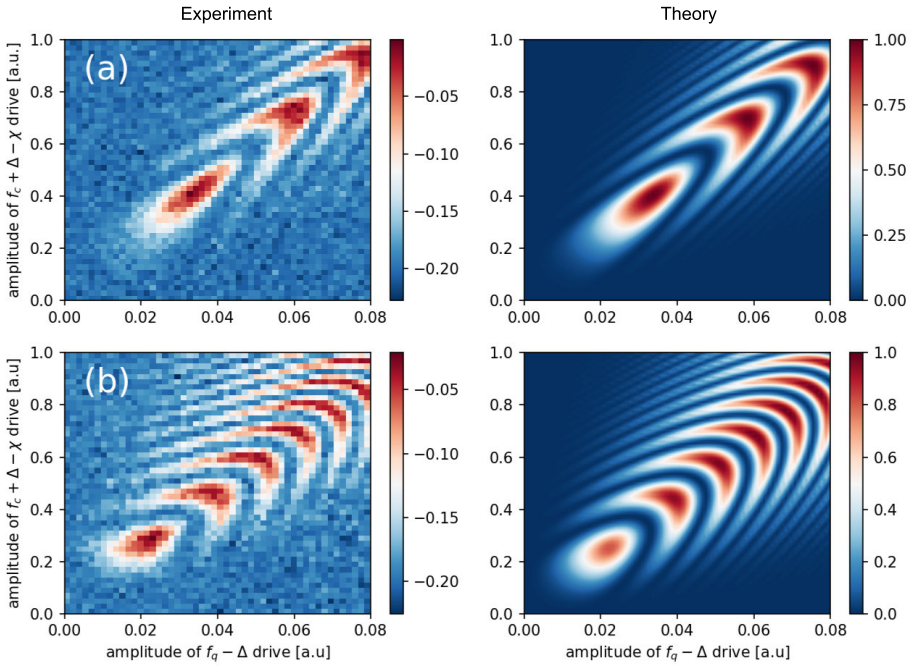

Figure 5.1: First calibration experiment in supplementary of paper VI. The excited population of the qubit in color scale for (a) transition $|0\rangle|g\rangle \rightarrow |1\rangle|e\rangle$ and (b) transition $|2\rangle|g\rangle \rightarrow |3\rangle|e\rangle$. The curving of the red areas is reproduced by a crosstalk term in the Stark shift in Eqs. 5.23 and 5.24.

For the purpose of fitting a part of the experimental data, we consider drives with the following drive frequencies

$$\omega_1 = \omega_q - \Delta, \tag{5.20}$$

$$\omega_2 = \omega_a - \chi + \Delta \tag{5.21}$$

Moving to the frame rotating with the free Hamiltonian and making the rotating wave approximation (RWA) allows selecting slow-rotating terms from the fourth-order interaction so that the Hamiltonian can be written as

$$\begin{aligned} H(t) &= \delta_{\text{Stark},q}\, q^\dagger q + \delta_{\text{Stark},a}\, a^\dagger a - \frac{\alpha_q}{2} q^{\dagger 2} q^2 - \frac{K_c}{2} a^{\dagger 2} a^2 - \chi q^\dagger q\, a^\dagger a \\ &+ \left(\xi_{\text{eff}}\, \mathrm{e}^{+i\, n\chi t} q^\dagger a^\dagger + \text{h.c.}\right). \end{aligned} \tag{5.22}$$

We are still working on fully reproducing the results of our experiments and the above Hamiltonian does not fully capture the results we measured. We can add here that in [102, 24] they use off-resonant drives and they find that their experimental data fits qualitatively rather than quantitatively their theoretical predictions.

To fit the experimental data in Fig. 5.1 with the model that we have, we find that a cross term in the Stark shifts (5.14) and (5.15) is needed. Assuming fitting parameters $\eta_1, \eta_2, \eta_{12}$, one can use (5.14) and (5.15) and write

$$\delta_{\text{Stark},q} = -2\,\eta_1\,\alpha_q\,|\xi_1|^2 - \eta_2\,\chi\,|\xi_2|^2 - \eta_{12}\,\chi\,\xi_1\,\xi_2, \tag{5.23}$$

$$\delta_{\text{Stark},a} = -2\,\eta_2\,K_c\,|\xi_2|^2 - \eta_1\,\chi\,|\xi_1|^2 - \eta_{12}\,\chi\,\xi_1\,\xi_2, \tag{5.24}$$

The experimental data in Fig. 5.1 is the first calibration experiment we do in order to find approximate amplitudes of the off-resonant drives for each transition $|n\rangle|g\rangle \to |n+1\rangle|e\rangle$ that we are interested in driving ($n = 0$ and $n = 2$ in Fig. 5.1(a) and (b) respectively). We apply a qubit drive at frequency $f_q - \Delta$ and a cavity drive at frequency $f_c + \Delta - (n+1)\chi$, where $\Delta = 20$ MHz. The red areas indicate the regions where the qubit is excited. The fitting parameters for both color plots are found to be

$$(\eta_1, \eta_2, \eta_{12}) = (3.75, 3.35, 60.25)\,. \tag{5.25}$$

Without the extra term the red areas do not bend to form arrow-like regions pointing to the top-right corner of the color plots (Fig. 5.1).

Even though we cannot fully describe the evolution of our system under off-resonant drives just yet, we can still apply selective photon additions experimentally. We just need to calibrate our pulses on the experiment itself. It turns out it is not a time-intensive calibration procedure and it is explained in detail in the Supplementary information of paper VI. Once we find the Hamiltonian that fully describes evolution under off-resonant drives we will be able to shorten the duration of selective photon addition gates by optimizing the envelopes of the off-resonant drives, similarly to what we did with the SNAP gates (see Sec. 4.5.2 and paper IV).

5.2 Experimental implementation of selective photon addition (Results summary)

We implement the selective photon addition gate in paper VI. We have a specific use for it in mind, namely correcting the single photon loss. However, this does not mean that the selective photon addition gate cannot be used for other purposes.

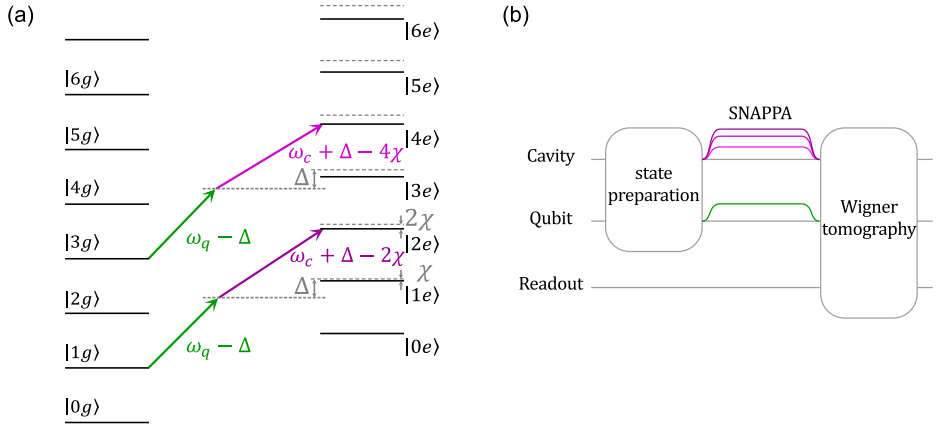

Figure 5.2: (a) Level diagram sketching the SNAPPA gate, here implemented to map the cavity odd parity subspace onto the even-parity subspace, without compromising the even-parity states. The qubit off-resonant drive at frequency $f_q - \Delta$ is common for all the transitions (green arrows). In different shades of magenta arrows, the cavity off-resonant drives at frequencies $f_c + \Delta - (n+1)\chi$ enable the transition from $|n\rangle|g\rangle$ to $e^{i\theta_n}|n+1\rangle|e\rangle$, for each odd n respectively. The phase θ_n is directly related to the relative phases of the drives. (b) Pulse sequence used to apply the SNAPPA gate. We initialize cavity and qubit to $|\Psi\rangle|g\rangle$, apply the SNAPPA gate, and perform direct Wigner tomography to measure the state of the cavity.

We can encode the logical qubit in a four-component cat state (same as in [25]) that has, for example, even parity. When a photon is lost, the parity of the logical states will change. We want our selective photon addition gate to leave the even parity states unchanged, and we want the odd parity states to be mapped back to even parity states. Our off-resonant drives will further put the qubit in the excited state if the parity has been changed, and leave it in the ground state if there was no parity change. They can also add an arbitrary phase to the added photons. This is why we call this gate selective number-dependent arbitrary phase photon addition or SNAPPA for short. It is defined as

$$S_{\mathrm{PA}}(\{(\theta_i)_{n_i \to n_{i+1}}\}) \equiv \sum_{i \subset N} e^{i\theta_i} |n_i + 1\rangle|e\rangle\langle n_i|\langle g| + \mathrm{h.c.}, \tag{5.26}$$

where $|n_i\rangle$ are the Fock states which are affected by the transformation when the qubit is in the ground state, $\{\theta_i\}$ the corresponding phases they acquire, and $|g\rangle$ and $|e\rangle$ are the ground and excited states of the qubit, respectively.

We will show all these properties by initiating cavity in equal su-

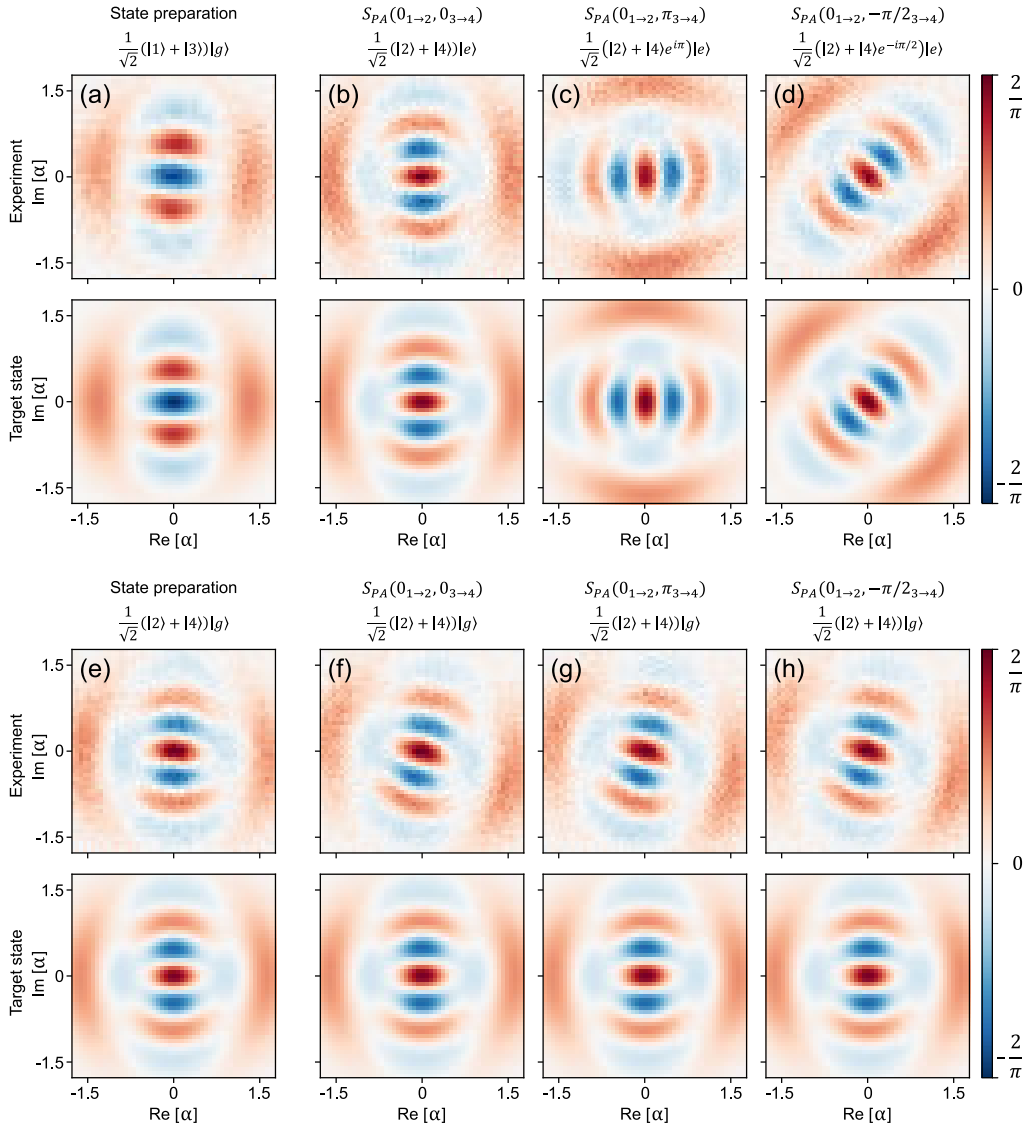

Figure 5.3: Characterization of the SNAPPA gate $S_{\mathrm{PA}}(\theta_{1\to2}, \theta_{3\to4})$, where $\theta_{1\to2} = 0$, to map odd-parity states(error), i.e., $\{|1\rangle, |3\rangle\}$ to even-parity states(computational), i.e., $\{|2\rangle, |4\rangle\}$, whereas the computational states are almost unaffected by the SNAPPA gate. Wigner functions of experimental versus target states when the SNAPPA gate is applied to an error initial state(upper panels) and a computational initial state(upper panels) confirms transition $|1\rangle|g\rangle \to |2\rangle|e\rangle$ and $|3\rangle|g\rangle \to |4\rangle|e\rangle$. (a) Error initial state $(|1\rangle + |3\rangle)|g\rangle/\sqrt{2}$ and final/target states $(|2\rangle + |4\rangle e^{i\theta_{3\to4}})|e\rangle/\sqrt{2}$, where $\theta_{3\to4}$ is the phase of the cavity off-resonant drive $f_c + \Delta - 4\chi$, given by (b) $\theta_{3\to4} = 0$, (c) $\theta_{3\to4} = \pi$, (d) $\theta_{3\to4} = \pi/2$. The lower panels show that the drives have little to no effect on the even-parity subspace. (e) Computational initial state $(|2\rangle + |4\rangle)|g\rangle/\sqrt{2}$ and (f)-(h) identical final state $(|2\rangle + |4\rangle)|g\rangle/\sqrt{2}$ for $\theta_{3\to4} = 0, \pi, -\pi/2$.

perposition of odd states $|\Psi\rangle = (|1\rangle + |3\rangle)/\sqrt{2}$ and even states $|\Psi\rangle = (|2\rangle + |4\rangle)/\sqrt{2}$ (Fig. 5.2). Then we will apply a SNAPPA gate that acts

on the states $|1\rangle$ and $|3\rangle$, $S_{\mathrm{PA}}(\theta_{1\to2}, \theta_{3\to4})$, with $\theta_{1\to2} = 0$ and $\theta_{3\to4}$ being an arbitrary phase. This phase is set by the relative phases of the off-resonant drives (see Fig. 5.2). We finally measure the Wigner function and the state of the qubit to characterize the state of the system after applying the SNAPPA gate.

The results are summarized in Fig. 5.3. When we initialize the cavity state in the odd parity state $(|1\rangle + |3\rangle)/\sqrt{2}$ and apply the SNAPPA gate $S_{\mathrm{PA}}(0_{1\to2}, \theta_{3\to4})$ we create the state $(|2\rangle + e^{i\theta_{3\to4}}|4\rangle)/\sqrt{2}$ and the qubit ends up in the excited state as expected (Fig. 5.3(a)-(d)). When we initialize the cavity state in the even parity state $(|2\rangle + |4\rangle)/\sqrt{2}$ and apply the same SNAPPA gate, the cavity state does not change, except for a slight rotation that is the same for all states, and the qubit ends up in the ground state as expected (Fig. 5.3(e)-(h)). Since the rotation is the same, we can easily compensate for it, by updating our knowledge of the qubit measurement outcome. The average error introduced in the qubit state population is about 0.05 and the average error introduced in the cavity state is about 0.02.

We can conclude that we successfully calibrated the SNAPPA gate and in the following chapter we will discuss the possible improvements and outlook for the application of the SNAPPA gate.

5.3 Open questions

There are a few open questions we would like to answer in the future. The obvious one is whether applying selective photon addition followed by an unconditional qubit reset would improve the lifetime of the bosonic qubit encoded in a four-component cat state or any other suitable code. There is still an option of whether to apply all the drives simultaneously (similar to [24]) or to do it in a more conventional pulsed manner where we do rounds of error correction repeatedly. The simultaneous option has the disadvantage of a more complicated calibration procedure, since it would involve more simultaneously applied drives. We do not know if the dives induce dephasing of either the qubit or the cavity. If the answer is yes, it would be better to apply them for short times in a pulsed manner.

We would obviously like to be able to find the Hamiltonian that fully describes the system driven by multiple off-resonant drives. This would allow us to shorten the duration of selective photon addition gates by optimizing the envelopes of the off-resonant drives, similarly to what we did with the SNAP gates (see Sec. 4.5.2 and paper IV). This would further improve the fidelity of the SNAPPA gates.

CHAPTER 6

Summary

In this thesis, we show how to build a bosonic microwave qubit in a 3D cavity. Starting from hardware components, moving on to techniques to shape bosonic states and gates, and proposing a novel single-photon error correction technique. We additionally introduce the experimental setup and room-temperature radio-frequency system on a chip we used to perform the measurements.

We first describe the cryogenic experimental setup and the sample fabrication common for all the experiments performed in this thesis. We discuss the room-temperature measurement and control systems we used for both bosonic and discrete variable qubit systems.

Next, we introduce the quality factor as a figure of merit we can use to compare the quality of resonators and qubits. We then present the different sources of loss that can limit the quality factor. Finally, we list the techniques used to analyze fluctuations of parameters both in the time and in the frequency domain.

In paper I relaxation and dephasing mechanisms of transmon qubits are studied over an extended time period. The analysis of fluctuations

of coherence times and resonance frequencies indicates that the parasitic two-level systems are the main cause of the instability of these parameters in time.

In paper II we measure the resonance frequency fluctuations of three different types of resonators. All the resonators' fluctuations show a signature of coupling to multiple two-level systems. The switching time and amplitude of the fluctuations of the strongest coupled two-level system have the same functional form of the power dependence in all three resonators indicating that TLSs are neither geometry nor material dependent.

In paper III we were focused on finding a good recipe for treating the surface of aluminum 3D cavities with the goal of reproducibly achieving quality factors close to 100 million. The best recipe we found includes wet etching that removes about 100 μm of the surface, which is affected by machining, followed by annealing in a nitrogen atmosphere for 3 hours to allow some of the defects to rearrange and heal.

Next, we focused on the universal control of a bosonic qubit. Dispersively coupling the ancilla qubit to the cavity was the way we chose to introduce the nonlinearity needed for universal control. We introduced the types of gates we can perform by resonantly driving the ancilla qubit and the cavity.

In paper IV we used interleaved displacement and optimized SNAP gates to create arbitrary Wigner-negative states such as Gottesman-Kitaev-Preskill (GKP) states and cubic phase states. We were able to do this by employing a two-step optimization process. In the first step, we optimized the parameters of the gates, and in the second step, we optimized the envelopes of SNAP gates in order to make them 8x shorter compared to the standard SNAP gates.

In paper V we then used the coherent state process tomography to fully characterize the bosonic X-gate on a binomially encoded qubit. The X-gate was implemented by interleaving 4 displacement and 3 optimized SNAP gates that were optimized in the way described in paper IV. The coherent state tomography is made practical by employing the gradient-

descend based learning algorithm that reconstructs the quantum process matrix from very limited data.

In chapter 5 and paper VI we explore driving the cavity-qubit system off-resonantly. In particular, we focus on the two-excitation transition that selectively adds a photon and excites the qubit at the same time. We explore the Hamiltonian description that would allow us to capture the Stark shifts induced by multiple off-resonant drives. By choosing the drives carefully and implementing a qubit reset, we believe we can implement a single photon error correction on a qubit encoded in a four-component cat state.

In paper VI we focus on calibrating the selective two-excitation transitions. When the two-excitation transitions implement a π pulse between levels $|ng\rangle$ and $|(n+1)e\rangle$ we call the gate selective number dependent arbitrary phase photon addition or SNAPPA for short.

In paper VII the measurement system on a chip Presto is used to characterize a discrete two-qubit transmon system. This is the same system used in paper VI to implement the SNAPPA gates.

APPENDIX A

Common calibration experiments

Papers IV-VI are all performed on the same system[1]. It consists of a 3D cavity dispersively coupled to the transmon qubit and a readout resonator. The Hamiltonian describing this system is given in Eq. 4.14. Next, we will go through all the experiments needed to calibrate the parameters of that Hamiltonian.

The frequency of the qubit ω_q is obtained from a Ramsey experiment (see Fig. A.1(a)). We send two $\pi/2$ pulses separated by a variable time. The result is an exponentially decaying oscillation at a frequency that corresponds to the difference frequency between the qubit frequency and the frequency of the $\pi/2$ pulses $\omega_{Ramsey} = \omega_q - \omega_{\pi/2}$. From the exponential decay we extract T_{2q} the decoherence time of the qubit

$$f(t) = e^{-t/T_{2q}} \cos\left[(\omega_q - \omega_{\pi/2})t\right]. \tag{A.1}$$

The frequency of the cavity we fit in a similar manner. We apply two displacements of opposite phase (D_α and $D_{-\alpha}$) separated by a variable time dt. The average photon number associated with the displacement amplitude has to be much smaller than 1 ($|\alpha|^2 \ll 1$) in order to use a

[1]This does not mean that the physical components were identical.

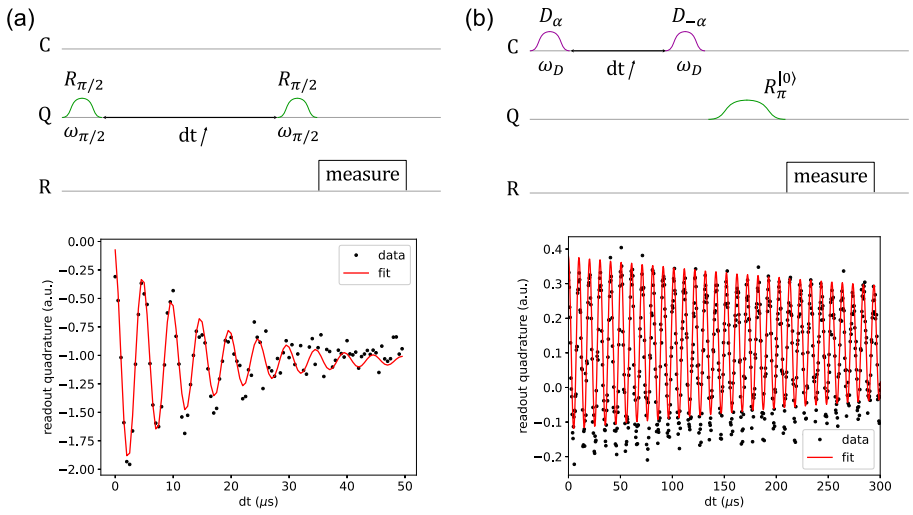

Figure A.1: Calibrating the frequency of the qubit (a) and the cavity (b). We use a Ramsey experiment that we fit to an exponentially decaying oscillation. The pulse sequence to perform the experiment (top) and an example of the measurement data with the fit (bottom).

simple exponentially decaying cosine as a fit. The difference between the frequency of the displacement pulses and the frequency of the cavity is going to determine the frequency of the cosine. We then apply a π pulse selective on cavity being in vacuum (see Fig. A.1(b)). One way to visualize why we are getting oscillations in this experiment is to think about it in phase space. The first displacement creates a coherent state $|\alpha\rangle$. Since the displacement frequency does not exactly match the frequency of the cavity, this displaced state is going to rotate around the origin of phase space with frequency $\omega_c - \omega_D$. So the state $|\alpha\rangle$ will evolve into $|\alpha e^{i(\omega_c - \omega_D)t}\rangle$. Depending on how much time has passed, by applying displacement $D_{-\alpha}$ we will either bring the state back to the vacuum state (for time $dt = 1/(\omega_c - \omega_D)$) and read high amplitude when we probe the population of the Fock state $|0\rangle$, or low probability to be in the vacuum state at times $dt = 1/[2(\omega_c - \omega_D)]$ when the displaced state evolved into state $|-\alpha\rangle$.

Measurements of the relaxation time of the qubit and the cavity are presented in Fig. A.2. The qubit relaxation time T_{1q} is measured by applying a π pulse to the qubit and waiting a variable time dt. The

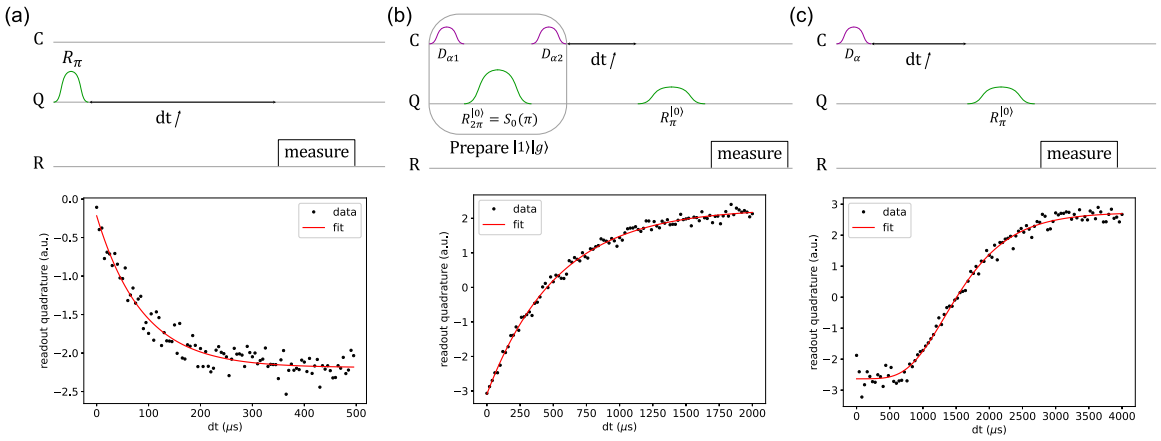

Figure A.2: Calibrating the relaxation time of the qubit (a), and the cavity (b) and (c). The pulse sequence to perform the experiment (top) and an example of the measurement data with the exponentially decaying fit (bottom). One way to prepare Fock state $|1\rangle$ is to apply displacement $\alpha_1 = 1.14$, SNAP gate that adds π phase to Fock state $|0\rangle$ and another displacement $\alpha_2 = -0.58$. $\alpha = 3.3$ is the displacement amplitude in the example in panel (c).

exponential decay of the qubit population is fitted to:

$$f(t) = e^{-t/T_{1q}}. \tag{A.2}$$

The cavity relaxation time T_{1c} can be measured in two ways. The first way is to prepare Fock state $|1\rangle$ and measure the population of either Fock state $|0\rangle$ or $|1\rangle$ after variable time dt. The population of Fock state $|1\rangle$ will exponentially decay and population of Fock state $|0\rangle$ will exponentially approach one with characteristic time T_{1c} (see Fig. A.2(b)). Another way is to prepare a coherent state α instead of Fock state $|1\rangle$. The population of Fock state $|0\rangle$ will then fit to a double exponential:

$$f(t) = \exp\left(-|\alpha|e^{-t/T_{1c}}\right). \tag{A.3}$$

The qubit drive amplitude is calibrated using the standard Rabi measurement (see Fig. A.3). For each amplitude in instrument units (arbitrary units, a.u.) we sweep the length of the qubit pulse. We fit the population of the qubit to a cosine function

$$f(t) = \cos\left(\omega_{Rabi}t - \pi/2\right). \tag{A.4}$$

and find the Rabi rate ω_{Rabi} corresponding to the instrument amplitude A in (a.u.). The dependence of $\omega_{Rabi}(A)$ is usually linear, except for

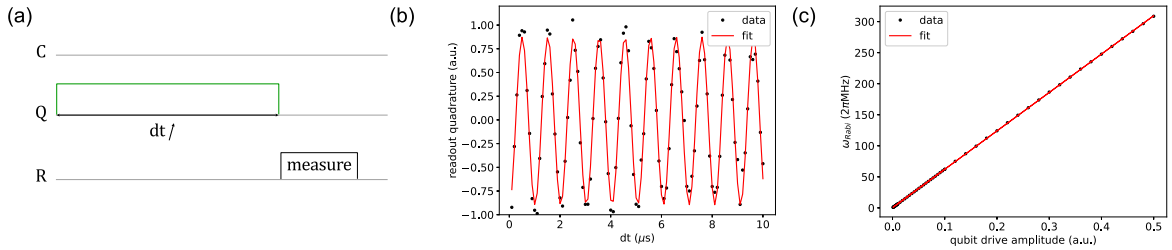

Figure A.3: Calibrating the qubit drive amplitudes. (a) pulse sequence, (b) example of Rabi oscillations for one amplitude of qubit drive, and (c) linear dependence of Rabi rate and qubit drive amplitude.

very high powers where there might be saturation effects or at very low powers where there might be nonlinearities caused by finite amplitude digitization. We use this measurement to convert the amplitudes we acquire from the optimizer when optimizing SNAP gate envelopes into instrument units.

The experiment detailed in Fig. A.4 is used to calibrate displacement amplitude, dispersive shift χ, and the correction to the dispersive shift χ'. We first apply a displacement pulse, and then we probe the population of the Fock states by applying a selective π pulse of varying frequency. We fit the individual peaks to Gaussian functions and the heights of the Gaussians to the Poisson distribution. This way we can find the linear relation between the displacement amplitude $|\alpha|$ and the voltage amplitude in arbitrary units that we apply. Further, the frequency of the peaks is fitted to

$$\omega(n) = \omega_q - \chi n - \frac{\chi'}{2} n(n-1). \tag{A.5}$$

Cavity Kerr K_c is very small in our system (few kHz) and on the same order as cavity relaxation time, so it is impossible to use spectroscopic methods. Instead, we do the same experiment as when we were determining cavity frequency, but now we also sweep the displacement amplitude (see Fig. A.5). If the cavity was perfectly linear we would see the red areas becoming more narrow as the displacement amplitude is increased. The cavity Kerr adds more phase to higher Fock states, and that is why we see the red areas bending as the displacement amplitude increases. The whole color plot is then fitted to find the cavity Kerr. The fitting

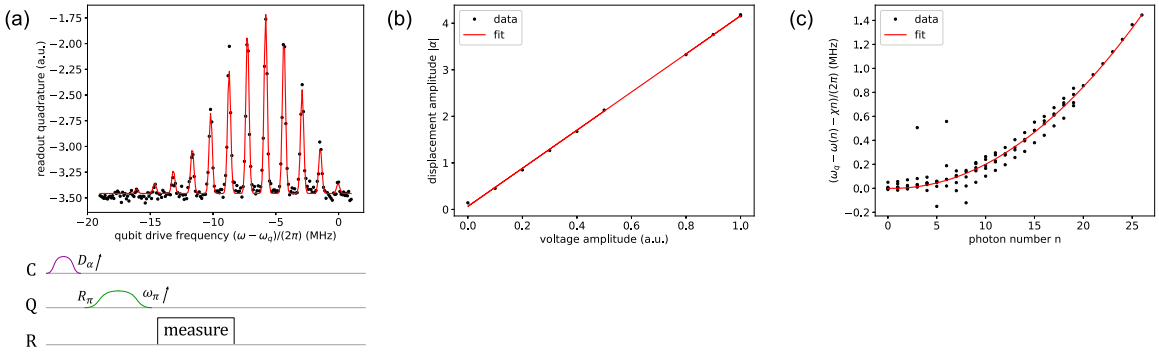

Figure A.4: Calibrating the cavity drive amplitudes. (a) Example of qubit frequency peaks whose heights fit the Poissonian distribution of a coherent state with amplitude α. (b) Linear dependence of displacement amplitude on cavity drive amplitude. (c) Frequencies of the peaks in (a) fitted to Eq. A.5 that allows us to extract dispersive shift χ and the correction to the dispersive shift χ'. Many points at the same photon number n correspond to extracting the position of the same peak for different displacement amplitudes D_α. (bottom) Pulse sequence for calibration displacement amplitude, dispersive shift, and the correction χ to the dispersive shift χ'.

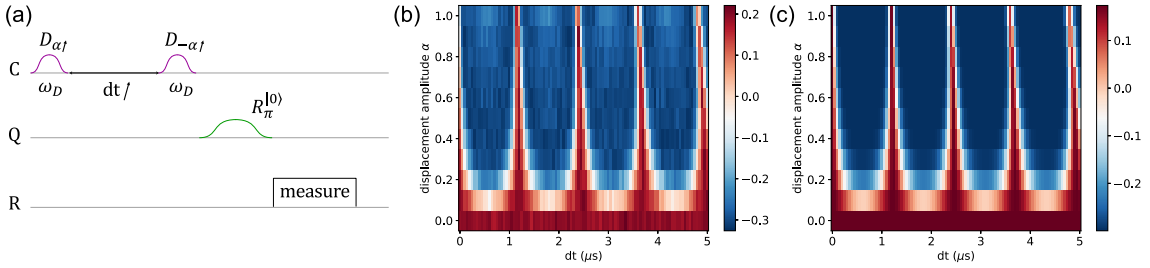

Figure A.5: Calibrating the cavity Kerr K_c. (a) Pulse sequence, (b) data, and (c) fit to Eq. A.6.

function computes the expression

$$f(\alpha, t) = \langle 0|D_{-\alpha} \prod_n e^{i\omega_\Delta t|n\rangle\langle n|} e^{i\frac{K_c}{2}n(n-1)t|n\rangle\langle n|} |\alpha\rangle \tag{A.6}$$

for every α and t in the 2D data set, and the only fitting parameters are K_c and the detuning from the cavity frequency $\omega_\Delta = \omega_D - \omega_c$. We choose the maximum time $dt \ll T_{2c}$ so we have negligible decay of amplitude, and ω_Δ such that we see a few oscillations.

Bibliography

[1] J. Chiaverini et al. "Realization of quantum error correction". *Nature* 432.7017 (2004), pp. 602–605.

[2] L. S. Madsen et al. "Quantum computational advantage with a programmable photonic processor". *Nature* 606.7912 (2022), pp. 75–81.

[3] M. Veldhorst et al. "A two-qubit logic gate in silicon". *Nature* 526.7573 (2015), pp. 410–414.

[4] N. W. Hendrickx et al. "A four-qubit germanium quantum processor". *Nature* 591.7851 (2021), pp. 580–585.

[5] A. Kinos et al. "Roadmap for rare-earth quantum computing". *arXiv:2103.15743* (2021).

[6] P. Krantz, M. Kjaergaard, F. Yan, T. P. Orlando, S. Gustavsson, and W. D. Oliver. "A quantum engineer's guide to superconducting qubits". *Applied Physics Reviews* 6 (2019), p. 021318.

[7] A. Blais, S. M. Girvin, and W. D. Oliver. "Quantum information processing and quantum optics with circuit quantum electrodynamics". *Nature Physics* 16.3 (2020), pp. 247–256.

[8] G. Wendin. "Quantum information processing with superconducting circuits: a review". *Reports on Progress in Physics* 80.10 (2017), p. 106001.

[9] F. Arute et al. "Quantum supremacy using a programmable superconducting processor". *Nature* 574.7779 (2019), pp. 505–510.

[10] Y. Wu et al. "Strong quantum computational advantage using a superconducting quantum processor". *Physical Review Letters* 127.18 (2021), p. 180501.

[11] *IBM processors with up to 127 qubits.* `https://quantum-computing.ibm.com/`. Accessed: 2022-12-20.

[12] P. W. Shor. "Algorithms for quantum computation: discrete logarithms and factoring". *Proceedings 35th annual symposium on foundations of computer science*. IEEE. 1994, pp. 124–134.

[13] L. K. Grover. "Quantum Mechanics Helps in Searching for a Needle in a Haystack". *Physical Review Letters* 79.2 (1997), pp. 325–328.

[14] M. H. Freedman. "Quantum computation and the localization of modular functors". *Foundations of Computational Mathematics* 1.2 (2001), pp. 183–204.

[15] S. B. Bravyi and A. Y. Kitaev. “Quantum codes on a lattice with boundary”. *arXiv:quant-ph/9811052* (1998).

[16] A. G. Fowler, M. Mariantoni, J. M. Martinis, and A. N. Cleland. “Surface codes: Towards practical large-scale quantum computation”. *Physical Review A* 86.3 (2012), p. 032324.

[17] S. Lloyd and S. L. Braunstein. “Quantum Computation over Continuous Variables”. *Physical Review Letters* 82.8 (1999), pp. 1784–1787.

[18] A. Joshi, K. Noh, and Y. Y. Gao. “Quantum information processing with bosonic qubits in circuit QED”. *Quantum Science and Technology* 6 (2021), p. 033001.

[19] W. Cai, Y. Ma, W. Wang, C.-L. Zou, and L. Sun. “Bosonic quantum error correction codes in superconducting quantum circuits”. *Fundamental Research* 1.1 (2021), pp. 50–67.

[20] M. Reagor et al. “Quantum memory with millisecond coherence in circuit QED”. *Physical Review B* 94 (2016), p. 014506.

[21] M. Reagor. “Superconducting Cavities for Circuit Quantum Electrodynamics”. PhD thesis. Yale University, 2015.

[22] A. Romanenko et al. “Three-Dimensional Superconducting Resonators at $T <$ 20 mK with Photon Lifetimes up to $\tau = 2$ s”. *Physical Review Applied* 13.3 (2020), p. 034032.

[23] B. Vlastakis et al. “Deterministically encoding quantum information using 100-photon Schrödinger cat states”. *Science* 342.6158 (2013), pp. 607–610.

[24] J. M. Gertler, B. Baker, J. Li, S. Shirol, J. Koch, and C. Wang. “Protecting a bosonic qubit with autonomous quantum error correction”. *Nature* 590 (2021), p. 243.

[25] N. Ofek et al. “Extending the lifetime of a quantum bit with error correction in superconducting circuits”. *Nature* 536 (2016), p. 441.

[26] M. H. Michael, M. Silveri, R. T. Brierley, V. V. Albert, J. Salmilehto, L. Jiang, and S. M. Girvin. “New Class of Quantum Error-Correcting Codes for a Bosonic Mode”. *Physical Review X* 6 (2016), p. 031006.

[27] L. Hu et al. “Quantum error correction and universal gate set operation on a binomial bosonic logical qubit”. *Nature Physics* 15.5 (2019), pp. 503–508.

[28] Z. Ni et al. “Beating the break-even point with a discrete-variable-encoded logical qubit”. *arXiv:2211.09319* (2022).

[29] D. Gottesman, A. Kitaev, and J. Preskill. “Encoding a qubit in an oscillator”. *Physical Review A* 64 (2001), p. 012310.

[30] P. Campagne-Ibarcq et al. “Quantum error correction of a qubit encoded in grid states of an oscillator”. *Nature* 584.7821 (2020), pp. 368–372.

[31] C. Flühmann, T. L. Nguyen, M. Marinelli, V. Negnevitsky, K. Mehta, and J. P. Home. “Encoding a qubit in a trapped-ion mechanical oscillator”. *Nature* 566 (2019), p. 513.

[32] V. Sivak et al. “Real-time quantum error correction beyond break-even”. *arXiv:2211.09116* (2022).

[33] W.-L. Ma, S. Puri, R. J. Schoelkopf, M. H. Devoret, S. M. Girvin, and L. Jiang. “Quantum control of bosonic modes with superconducting circuits”. *Science Bulletin* 66.17 (2021), pp. 1789–1805.

[34] M. Scigliuzzo. “Effects of the environment on quantum systems”. PhD thesis. Chalmers University of Technology, 2021.
[35] D. Niepce. “Superinductance and Fluctuating Two-lewel Systems”. PhD thesis. Chalmers University of Technology, 2020.
[36] D. Pozar. *Microwave Engineering, 4th Edition*. Wiley, 2011.
[37] E. M. Purcell. “Spontaneous emission probabilities at radio frequencies”. In: *Confined Electrons and Photons*. Springer, 1995, pp. 839–839.
[38] S. Probst, F. B. Song, P. A. Bushev, A. V. Ustinov, and M. Weides. “Efficient and robust analysis of complex scattering data under noise in microwave resonators”. *Review of Scientific Instruments* 86 (2015), p. 024706.
[39] C. Wang et al. “Surface participation and dielectric loss in superconducting qubits”. *Applied Physics Letters* 107.16 (2015), p. 162601.
[40] A. D. O’Connell et al. “Microwave dielectric loss at single photon energies and millikelvin temperatures”. *Applied Physics Letters* 92.11 (2008), p. 112903.
[41] P. Macha, S. van Der Ploeg, G. Oelsner, E. Il’ichev, H.-G. Meyer, S. Wünsch, and M. Siegel. “Losses in coplanar waveguide resonators at millikelvin temperatures”. *Applied Physics Letters* 96.6 (2010), p. 062503.
[42] J. M. Martinis et al. “Decoherence in Josephson Qubits from Dielectric Loss”. *Physical Review Letters* 95.21 (2005), p. 210503.
[43] S. Schlör et al. “Correlating Decoherence in Transmon Qubits: Low Frequency Noise by Single Fluctuators”. *Physical Review Letters* 123.19 (2019), p. 190502.
[44] P. V. Klimov et al. “Fluctuations of Energy-Relaxation Times in Superconducting Qubits”. *Physical Review Letters* 121.9 (2018), p. 090502.
[45] D. C. Mattis and J. Bardeen. “Theory of the anomalous skin effect in normal and superconducting metals”. *Physical Review* 111.2 (1958), p. 412.
[46] J. Gao. “The physics of superconducting microwave resonators”. PhD thesis. California Institute of Technology, 2008.
[47] L. Grünhaupt et al. “Loss mechanisms and quasiparticle dynamics in superconducting microwave resonators made of thin-film granular aluminum”. *Physical Review Letters* 121.11 (2018), p. 117001.
[48] D. Gusenkova et al. “Operating in a deep underground facility improves the locking of gradiometric fluxonium qubits at the sweet spots”. *Applied Physics Letters* 120.5 (2022), p. 054001.
[49] A. Megrant et al. “Planar superconducting resonators with internal quality factors above one million”. *Applied Physics Letters* 100.11 (2012), p. 113510.
[50] G. Calusine et al. “Analysis and mitigation of interface losses in trenched superconducting coplanar waveguide resonators”. *Applied Physics Letters* 112.6 (2018), p. 062601.
[51] M. Reagor et al. “Reaching 10 ms single photon lifetimes for superconducting aluminum cavities”. *Applied Physics Letters* 102.19 (2013), p. 192604.
[52] K. I. Park. *Fundamentals of Probability and Stochastic Processes with Applications to Communications*. Springer, 2018.
[53] D. W. Allan. “Statistics of atomic frequency standards”. *Proceedings of the IEEE* 54.2 (1966), pp. 221–230.

[54] J. Snyder. “An ultra-high resolution frequency meter”. *Thirty Fifth Annual Frequency Control Symposium*. IEEE. 1981, pp. 464–469.

[55] C. M. Van Vliet and P. H. Handel. “A new transform theorem for stochastic processes with special application to counting statistics”. *Physica A: Statistical Mechanics and its Applications* 113.1-2 (1982), pp. 261–276.

[56] D. Salvino, S. Rogge, B. Tigner, and D. Osheroff. “Low temperature ac dielectric response of glasses to high dc electric fields”. *Physical Review Letters* 73.2 (1994), p. 268.

[57] S. Ludwig, P. Nalbach, D. Rosenberg, and D. Osheroff. “Dynamics of the destruction and rebuilding of a dipole gap in glasses”. *Physical Review Letters* 90.10 (2003), p. 105501.

[58] P. De Visser, J. Baselmans, P. Diener, S. Yates, A. Endo, and T. Klapwijk. “Number fluctuations of sparse quasiparticles in a superconductor”. *Physical Review Letters* 106.16 (2011), p. 167004.

[59] D. Ristè, C. Bultink, M. J. Tiggelman, R. N. Schouten, K. W. Lehnert, and L. DiCarlo. “Millisecond charge-parity fluctuations and induced decoherence in a superconducting transmon qubit”. *Nature Communications* 4.1 (2013), pp. 1–6.

[60] J. Burnett et al. “Evidence for interacting two-level systems from the 1/f noise of a superconducting resonator”. *Nature Communications* 5.1 (2014), pp. 1–6.

[61] P. Macha, S. van Der Ploeg, G. Oelsner, E. Il’ichev, H.-G. Meyer, S. Wünsch, and M. Siegel. “Losses in coplanar waveguide resonators at millikelvin temperatures”. *Applied Physics Letters* 96.6 (2010), p. 062503.

[62] A. Romanenko and D. Schuster. “Understanding quality factor degradation in superconducting niobium cavities at low microwave field amplitudes”. *Physical Review Letters* 119.26 (2017), p. 264801.

[63] L. Faoro and L. B. Ioffe. “Internal loss of superconducting resonators induced by interacting two-level systems”. *Physical Review Letters* 109.15 (2012), p. 157005.

[64] L. Faoro and L. B. Ioffe. “Interacting tunneling model for two-level systems in amorphous materials and its predictions for their dephasing and noise in superconducting microresonators”. *Physical Review B* 91.1 (2015), p. 014201.

[65] P. Welch. “The use of fast Fourier transform for the estimation of power spectra: a method based on time averaging over short, modified periodograms”. *IEEE Transactions on audio and electroacoustics* 15.2 (1967), pp. 70–73.

[66] A. Eickbusch et al. “Fast universal control of an oscillator with weak dispersive coupling to a qubit”. *Nature Physics* 18 (2022), pp. 1464–1469.

[67] H. Paik et al. “Observation of high coherence in Josephson junction qubits measured in a three-dimensional circuit QED architecture”. *Physical Review Letters* 107.24 (2011), p. 240501.

[68] D. L. Creedon, Y. Reshitnyk, W. Farr, J. M. Martinis, T. L. Duty, and M. E. Tobar. “High Q-factor sapphire whispering gallery mode microwave resonator at single photon energies and millikelvin temperatures”. *Applied Physics Letters* 98.22 (2011), p. 222903.

[69] C. Axline et al. “An architecture for integrating planar and 3D cQED devices”. *Applied Physics Letters* 109.4 (2016), p. 042601.

[70] M. Hofheinz et al. “Synthesizing arbitrary quantum states in a superconducting resonator”. *Nature* 459.7246 (2009), pp. 546–549.

[71] P. J. Leek, M. Baur, J. Fink, R. Bianchetti, L. Steffen, S. Filipp, and A. Wallraff. “Cavity quantum electrodynamics with separate photon storage and qubit readout modes”. *Physical Review Letters* 104.10 (2010), p. 100504.

[72] P. Reinhold, S. Rosenblum, W.-L. Ma, L. Frunzio, L. Jiang, and R. J. Schoelkopf. “Error-corrected gates on an encoded qubit”. *Nature Physics* 16.8 (2020), pp. 822–826.

[73] Y. Ma et al. “Error-transparent operations on a logical qubit protected by quantum error correction”. *Nature Physics* 16.8 (2020), pp. 827–831.

[74] T. Brecht et al. “Micromachined integrated quantum circuit containing a superconducting qubit”. *Physical Review Applied* 7.4 (2017), p. 044018.

[75] Z. K. Minev et al. “Planar multilayer circuit quantum electrodynamics”. *Physical Review Applied* 5.4 (2016), p. 044021.

[76] D. Zoepfl, P. R. Muppalla, C. Schneider, S. Kasemann, S. Partel, and G. Kirchmair. “Characterization of low loss microstrip resonators as a building block for circuit QED in a 3D waveguide”. *AIP Advances* 7.8 (2017), p. 085118.

[77] C. U. Lei, L. Krayzman, S. Ganjam, L. Frunzio, and R. J. Schoelkopf. “High coherence superconducting microwave cavities with indium bump bonding”. *Applied Physics Letters* 116.15 (2020), p. 154002.

[78] S. Krastanov et al. “Universal control of an oscillator with dispersive coupling to a qubit”. *Physical Review A* 92 (2015), p. 040303.

[79] T. Hillmann, F. Quijandría, G. Johansson, A. Ferraro, S. Gasparinetti, and G. Ferrini. “Universal gate set for continuous-variable quantum computation with microwave circuits”. *Physical Review Letters* 125.16 (2020), p. 160501.

[80] B. D. Josephson. “Possible new effects in superconductive tunnelling”. *Physics letters* 1.7 (1962), pp. 251–253.

[81] Y. Nakamura, Y. A. Pashkin, and J. Tsai. “Coherent control of macroscopic quantum states in a single-Cooper-pair box”. *Nature* 398.6730 (1999), pp. 786–788.

[82] J. Koch et al. “Charge-insensitive qubit design derived from the Cooper pair box”. *Physical Review A* 76 (2007), p. 042319.

[83] E. T. Jaynes and F. W. Cummings. “Comparison of quantum and semiclassical radiation theories with application to the beam maser”. *Proceedings of the IEEE* 51.1 (1963), pp. 89–109.

[84] W. Pfaff et al. “Controlled release of multiphoton quantum states from a microwave cavity memory”. *Nature Physics* 13.9 (2017), pp. 882–887.

[85] P. Magnard et al. “Fast and unconditional all-microwave reset of a superconducting qubit”. *Physical Review Letters* 121.6 (2018), p. 060502.

[86] C. Berdou et al. “One hundred second bit-flip time in a two-photon dissipative oscillator”. *arXiv:2204.09128* (2022).

[87] P. Reinhold. “Controlling Error-Correctable Bosonic Qubits”. PhD thesis. Yale University, 2019.

[88] A. Mari and J. Eisert. “Positive Wigner Functions Render Classical Simulation of Quantum Computation Efficient”. *Physical Review Letters* 109.23 (2012), p. 230503.

[89] V. Veitch, C. Ferrie, D. Gross, and J. Emerson. “Negative quasi-probability as a resource for quantum computation”. *New Journal of Physics* 14.11 (2012), p. 113011.

[90] K. Banaszek, G. D’ariano, M. Paris, and M. Sacchi. “Maximum-likelihood estimation of the density matrix”. *Physical Review A* 61.1 (1999), p. 010304.

[91] S. Ahmed, C. Sánchez Muñoz, F. Nori, and A. F. Kockum. “Quantum State Tomography with Conditional Generative Adversarial Networks”. *Physical Review Letters* 127 (2021), p. 140502.

[92] S. Ahmed, C. Sánchez Muñoz, F. Nori, and A. F. Kockum. “Classification and reconstruction of optical quantum states with deep neural networks”. *Physical Review Research* 3 (2021), p. 033278.

[93] T. Fösel, S. Krastanov, F. Marquardt, and L. Jiang. “Efficient cavity control with SNAP gates”. *arXiv:2004.14256* (2020).

[94] R. W. Heeres et al. “Cavity State Manipulation Using Photon-Number Selective Phase Gates”. *Physical Review Letters* 115 (2015), p. 137002.

[95] Application notes. *Designing fast optimal SNAP gates in superconducting resonators*. [Online; accessed 21.12.2022.] 2021.

[96] R. W. Heeres, P. Reinhold, N. Ofek, L. Frunzio, L. Jiang, M. H. Devoret, and R. J. Schoelkopf. “Implementing a universal gate set on a logical qubit encoded in an oscillator”. *Nature Communications* 8 (2017), p. 94.

[97] A. Kofman and A. Korotkov. “Two-qubit decoherence mechanisms revealed via quantum process tomography”. *Physical Review A* 80.4 (2009), p. 042103.

[98] E. Knill et al. “Randomized benchmarking of quantum gates”. *Physical Review A* 77.1 (2008), p. 012307.

[99] M. Lobino, D. Korystov, C. Kupchak, E. Figueroa, B. C. Sanders, and A. Lvovsky. “Complete characterization of quantum-optical processes”. *Science* 322.5901 (2008), pp. 563–566.

[100] S. Rahimi-Keshari, A. Scherer, A. Mann, A. T. Rezakhani, A. Lvovsky, and B. C. Sanders. “Quantum process tomography with coherent states”. *New Journal of Physics* 13.1 (2011), p. 013006.

[101] S. Ahmed, F. Quijandrıa, and A. F. Kockum. “Gradient-descent quantum process tomography by learning Kraus operators”. *arXiv:2208.00812* (2022).

[102] P. Campagne-Ibarcq et al. “Deterministic Remote Entanglement of Superconducting Circuits through Microwave Two-Photon Transitions”. *Physical Review Letters* 120.20 (2018), p. 200501.